A New View of the Lunar South Pole from the Lunar Orbiter Laser Altimeter (LOLA)

Michael K. Barker[a], Erwan Mazarico[a], Gregory A. Neumann[a], David E. Smith[b], Maria T. Zuber[b], James W. Head[c], Xiaoli Sun[a]

[a]NASA Goddard Space Flight Center, 8800 Greenbelt Rd., Greenbelt, MD 20771, USA
[b]Department of Earth, Atmospheric, and Planetary Sciences, MIT, Cambridge, MA, 02139, USA
[c]Department of Earth, Environmental and Planetary Sciences, Brown University, Providence, RI 02912, USA

Abstract

Upcoming missions to the lunar south pole require detailed maps over large areas to fully characterize landing sites locally and regionally and to place their data into proper geologic context. To that end, we enhanced the Lunar Orbiter Laser Altimeter (LOLA) altimetry dataset for the south polar region, from which we produced new maps of topography, topographic roughness, and permanently shadowed regions (PSRs). The roughness maps reveal a diversity of terrains characterized by hectometer-scale roughness which is controlled in this region primarily by cratering and downslope mass transport. The south polar region is littered with linear roughness features of order ~1 – 10 km wide and ~10s – 100s of km long hypothesized to be secondary impacts within extended ejecta rays. Non-uniformities in these features could reflect variations in secondary impactor properties and/or target terrain properties. Poleward of 80° S, the PSR cumulative size-frequency distribution (CSFD) shows an approximately power-law behavior whose exponent has a spatial variation of ~10%. PSRs with areas < 1 km^2 contain 15 ± 5% of the total PSR area. Finally, we studied the effect of false positives and false negatives on the accuracy of the measured PSR cumulative size-frequency distribution (CSFD) and on the area for any individual PSR. The new maps presented here have many applications in the science and exploration of the lunar south polar region, such as geologic mapping and traverse planning.

1 Introduction

Due to the Moon's low obliquity and heavily cratered terrain, its polar regions experience extreme illumination and temperature conditions within relatively short distances. Peaks of near-eternal sunlight tower above nearby permanently shadowed regions (PSRs) where water and other volatiles can be stable on or just below the surface for billions of years. This makes the polar regions important for establishing a long-term human presence and for answering fundamental science questions such as understanding the history of volatiles in the inner solar system. The lunar south polar region has become a high priority target for scientific investigation and both robotic and human exploration (NASEM, 2022). Indeed, many robotic and human missions are planned for the south pole over the next decade including NASA's Artemis III lunar landing and astronaut exploration mission.

Precise and accurate topographic maps, and their derived products, are critical inputs to many aspects of mission design (Heldmann et al. 2016). Mission planning requires knowledge of the topography on a variety of scales within and surrounding PSRs in order to fully characterize candidate landing sites locally and regionally. The Lunar Reconnaissance Orbiter (LRO) Lunar Orbiter Laser Altimeter (LOLA) altimetric dataset, with ~5 m altimetric footprints, provides the geodetic framework with which other lunar datasets can accurately co-register their data (Smith et al. 2017). LOLA data products also inform landing site characterization by providing surface height, slope, roughness, reflectance, and illumination (e.g., Mazarico et al. 2011; Rosenburg et al. 2011; Kreslavsky et al. 2013; Lemelin et al. 2016a; Smith et al. 2017).

One example of a LOLA derived product that has science and exploration applications is topographic roughness. Numerous studies have examined the topographic roughness properties of the Moon on a variety of scales (e.g., Rosenburg et al. 2011; Kreslavsky et al. 2013; Yokota et al. 2014; Lemelin et al. 2020; Wang et al. 2020, Deutsch et al. 2021; Cai & Fa 2020). Different processes govern the roughness on hectometer and kilometer-scales. Regolith gardening and hectometer- and smaller-scale impacts dominate hectometer-scale roughness. Bedrock-altering processes, like larger impacts, volcanism, and tectonism govern the roughness on kilometer scales (Kreslavsky et al. 2013**;** Lemelin et al. 2020). Moreover, in the polar regions, subsurface ice may alter the morphologies of craters and topographic roughness (Rubanenko et al. 2019; Deutsch et al. 2021; Moon et al. 2021).

In addition, topographic roughness is an important factor in determining the abundance of so-called "micro cold traps", regions $\lesssim$ 10 m in size that are cold enough to potentially host volatiles for geologic timescales (Hayne et al. 2021). These regions are of particular interest as they may be more numerous and more accessible than the canonical ~10 km size PSRs, such as those in Shackleton, Haworth, Shoemaker, and Faustini (e.g., Zuber et al. 2012; Tye et al. 2015). However, due to their small size, micro cold traps are difficult to fully characterize from orbit. Larger cold traps with sizes of order ~10

– 100 m are already resolvable with extant datasets including LOLA's, and therefore offer an attractive compromise between abundance and observability with remote sensing data.

Track geolocation errors a few meters horizontally and < 1 m vertically remaining from the precise LRO orbit determination (Mazarico et al. 2018) can cause spurious artifacts in a LOLA digital elevation model (LDEM). Previously, Barker et al. (2021) mitigated these artifacts through an iterative track adjustment process to derive new 5 m/pix topographic models for several south polar sites selected for their high illumination conditions. Here, we build upon that work to make new, improved altimetric profiles and maps, including uncertainty estimates, over larger areas (out to 30° from the south pole) and at different pixel scales (10 m/pix to 240 m/pix). From these new products, we produce roughness maps over a series of baselines and examine their geological characteristics and implications. We also derive a new, improved map of PSRs at 20 m/pix, the smallest pixel scale to date and, for the first time, quantify its uncertainties.

This paper is organized as follows. In Section 2, we describe the derivation of improved altimetry and topographic models for the lunar south pole. Then, in Section 3, we perform several validation checks and compute maps of uncertainty for surface height and slope. In Section 4, we derive roughness maps on hectometer and kilometer scales and examine their geological implications. In Section 5, we derive a new and improved PSR map and study the PSR statistics and accuracy. Finally, we summarize the results in Section 6.

2 New Topographic Models

Due to LRO's polar orbit, the LOLA data point density generally increases closer to the pole. For this reason, the LOLA polar gridded data products on the Planetary Data System (PDS; https://imbrium.mit.edu/) are nested in a hierarchical nature with larger-area LDEMs having larger pixel scales (Table 1). As the LRO orbit has evolved over the mission duration, some regions have received greater coverage than others even at the same latitude. Figure 1 shows how the effective resolution varies within 10° of the south pole. We define the effective resolution as the diameter of the largest circle that can fit between nearby LOLA spots or, equivalently, the largest crater diameter that would not be sampled by LOLA's spots. The patterns in the effective resolution map are likely affected by detection efficiency variations due to range variation and the thermal blanket anomaly (Smith et al. 2017), as well as normal instrument aging. Much of the Artemis zone (i.e., poleward of 84° S) has an effective resolution of ~20 m/pix. Therefore, the reference topographic product in this study is the 80° – 90° 20 m/pix south polar LDEM, although we update the other products as well. All the LOLA polar products use a stereographic projection centered at the pole in the MOON_ME frame of the JPL ephemeris DE421 (Williams et al. 2008; Folkner et al. 2009) to be consistent with the LRO project's conventions. Coordinates in the MOON_ME frame of DE421 have an overall uncertainty of a few meters relative to the

principal axis frame (Williams et al. 2008).

Table 1: LOLA polar gridded data products				
Old name	New name	Max latitude (° S)	Stereographic range (km)	Pixel scale (m/pix)
LDEM_85S_10M	LDEM_83S_10MPP_ADJ	85 (old) / 83 (new)	± 151.68 / ± 216.4	10
LDEM_80S_20M	LDEM_80S_20MPP_ADJ	80	± 304	20
LDEM_80S_40M	LDEM_80S_40MPP_ADJ	80	± 304	40
LDEM_80S_80M	LDEM_80S_80MPP_ADJ	80	± 304	80
LDEM_75S_30M	LDEM_75S_30MPP_ADJ	75	± 457.44	30
LDEM_60S_60M	LDEM_60S_60MPP_ADJ	60	± 931.2	60
LDEM_60S_120M	LDEM_60S_120MPP_ADJ	60	± 931.2	120
LDEM_60S_240M	LDEM_60S_240MPP_ADJ	60	± 931.2	240

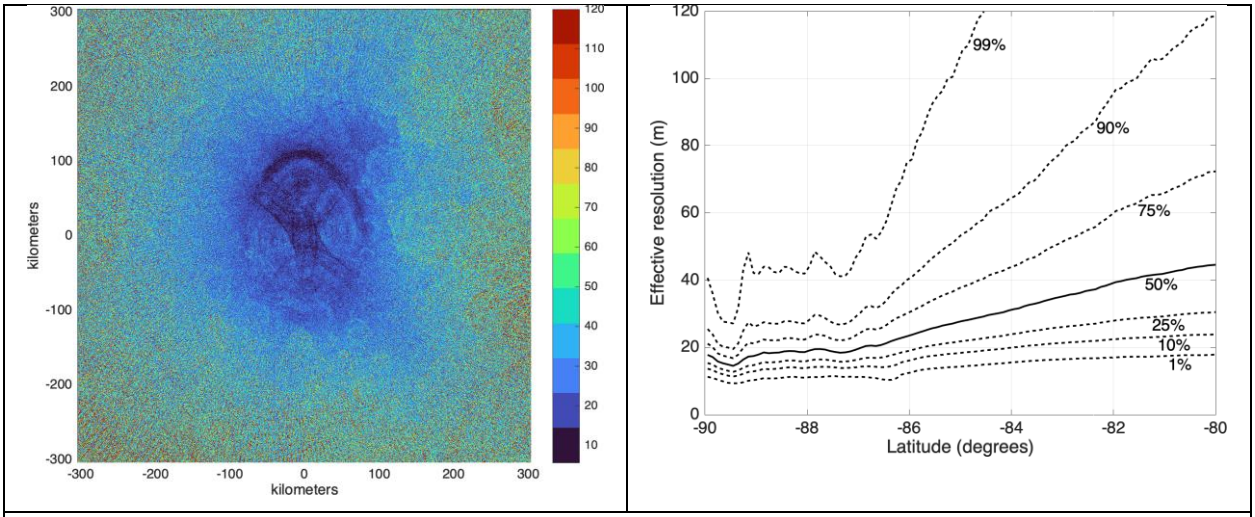

Figure 1 – Left panel: Map of effective resolution (in meters**,** binned at 80 m/pix) defined as the largest crater diameter that would not be sampled by LOLA. For this and all map-projected figures, the map projection is stereographic centered at the pole. Scale is true at the pole, with a projection radius of 1737.4 km. Right panel: Due to LRO's evolving polar orbit, the effective resolution increases toward the pole while some areas have received greater coverage than others even at the same latitude, as evident from the larger range in the percentile curves.

In previous work, LDEMs were cleaned by adjusting the LOLA tracks to a reference topographic model constructed from the LOLA tracks themselves (Zuber et al. 2012; Barker et al. 2021) or from stereophotogrammetry (Gläser et al. 2018). Here, we use the LOLA tracks themselves (i.e., the altimetric surface height measurements in the Reduced Data Records) to construct the reference basemap in an iterative fashion following a similar procedure as in Barker et al. (2021). We divide the 80° – 90° S 20 m/pix LDEM into 64 tiles, each 80 km on a side with 2 km overlaps between tiles. Due to the aforementioned polar orbit, the track density varies significantly over the total area, ranging from ~1500 to ~12,500 tracks per tile. The resulting fill factor (percentage of 20-m pixels with at least one LOLA spot) ranges from ~15% to ~75%. The track adjustment and cleaning process is run on each tile independently. In summary, for each tile, we randomly remove 2% of the tracks from the current best reference LDEM, adjust each of the removed tracks individually to the resulting "reduced" LDEM by applying 3-dimensional offsets and minimizing the root-mean-squared (RMS) surface height residuals between each individual laser return (referred to here as a point or spot) and the surface height at that location on the current reduced LDEM. The RMS residuals are typically ~1 – 2 m with a median absolute deviation (MAD) of ~0.35 – 0.50 m. This step is then repeated until all tracks have been adjusted. The process of running 50 batches until all tracks are adjusted is repeated 5 times in total, each time starting from a new LDEM computed with the best-fit track adjustments from the previous iteration. Outlying points are down-weighted during the track fitting to ensure they do not bias the results, and are removed after the final iteration.

In this work, all LDEM pixels (filled or unfilled) are assigned height values with the natural neighbor interpolation method that weights nearby LOLA points according to their Delaunay triangulation (Sibson 1981; Abramov & McEwen 2004; Bater & Coops 2009). This method is less susceptible to sub-pixel sampling errors than a simple median operation as done for previous LDEM products. A small percentage of isolated invalid LOLA returns and streaks of a few consecutive poor-quality returns are identified and removed in an automated fashion if they have an abnormally high slope or lie in runs of large residuals. In total, of order ~0.1% of all points are removed by this last step.

The cleaned point cloud tiles are then individually aligned to the original LDEM with a 3-D translation using the Ames Stereo Pipeline's *pc_align* tool (Beyer et al. 2018). This step preserves the overall geodetic accuracy of the map, as the original LDEM was constructed directly from the LRO orbits reconstructed from the radio tracking data using the GEODYN II orbit determination software (Pavlis and Nicholas, 2017). The translation vectors have a mean horizontal magnitude of 0.76 ± 0.29 m and a mean radial magnitude of 0.32 ± 0.08 m. The aligned and gridded point clouds are then blended together with a cosine taper weight in the overlap regions using the Generic Mapping Tools *grdblend* utility (Wessell et al. 2013). The counts maps (LDEC**;** number of LOLA spots per pixel) of the individual tiles are blended in the same way. Hence, non-integer counts can exist in the overlap regions of the final mosaicked product.

After applying these offsets, the difference in pixel height values between the tiles in their overlap regions has a mean and standard deviation of 0.00 ± 0.70 m with a median absolute value of 0.12 m.

As explained above, the polar LDEM products publicly available on the PDS are nested maps with decreasing resolution and increasing areal extent. To make new versions of these other maps outside the 80° – 90°S 20 m/pix LDEM region, we averaged each track's offsets after splitting them into day/night subsets to account for LOLA's thermal blanket anomaly (Smith et al. 2017). These offsets were then applied uniformly to each track's day/night portions over 60° – 90°S. Then, invalid returns were removed using the same slope and run criteria described above. For 10 m/pix and 30 m/pix, these day/night-adjusted and cleaned tracks were then gridded with natural neighbor interpolation. For larger pixel scales, the tracks were gridded first at 20 m/pix and then downsampled by multi-pixel averaging to 40, 60, 80, 120, and 240 m/pix. For these larger pixel sizes, this approach ensures that the pixel height values remain representative of the mean height within their pixels.

3 Validation and Uncertainties

Figure 2 shows a close-up of the Connecting Ridge (Site 01 in Barker et al. 2021) comparing the old (PDS) version (left panel) and the new version (right panel) of the 20 m/pix LDEM. Figures A1 – A10 show additional examples. The track adjustment and cleaning process has removed the majority of artifacts although some still do remain. We have attempted to strike a balance between under-cleaning and over-cleaning. The largest improvements occur over high slopes because, as slope increases, a constant horizontal geolocation error translates to a large vertical error in surface height.

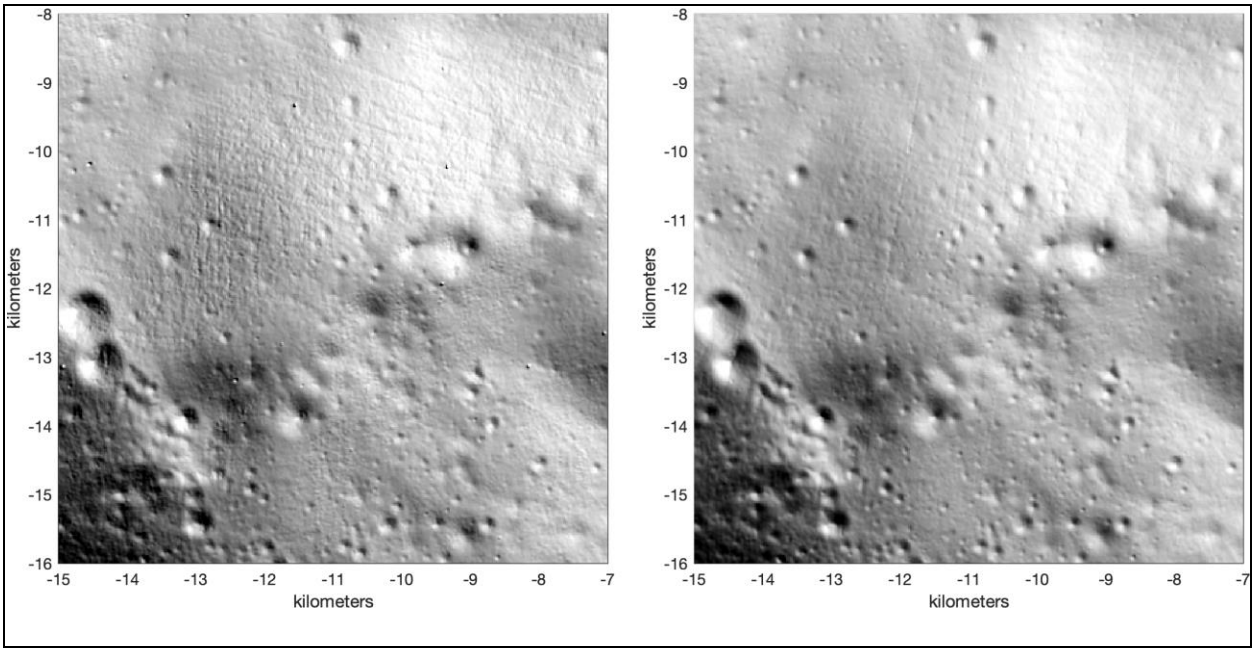

Figure 2 – Hillshade of old (left) and new (right) 20 m/pix LDEM.

Additional qualitative validation is achieved through comparison of LRO Narrow Angle Camera (NAC) images (whose locations are shown in Figure A11) to rendered images using the 20 m/pix LDEM and a 3-D ray-tracing algorithm (Mazarico et al. 2018). The surface is assumed here to be Lambertian with broadband visual albedo of 0.1. Figures 3 – 4 and Figures A12 – A18 show (a) the NAC image, (b) the corresponding rendered image, (c) effective resolution, and (d) counts.

These image-to-model comparisons show a good overall correspondence between the NAC and LDEM-rendered images. The highest level of detail is seen in the rendered images when the effective resolution is best, such as in Figure 3. On the other hand, Figure 4 shows how, when the LOLA point density is relatively low, large gaps between tracks appear as smooth surfaces in the rendered image. This figure also has examples of spurious noise points that remain in the new maps and that can appear as ‘flag-poles’ (labeled A and B) or ‘pot-holes’ (labeled C). In terms of the pixel values themselves, the LDEM-rendered image radiance factor (I/F) has a typical RMS error of ~30%, which is reasonable given the assumed constant-albedo Lambertian surface.

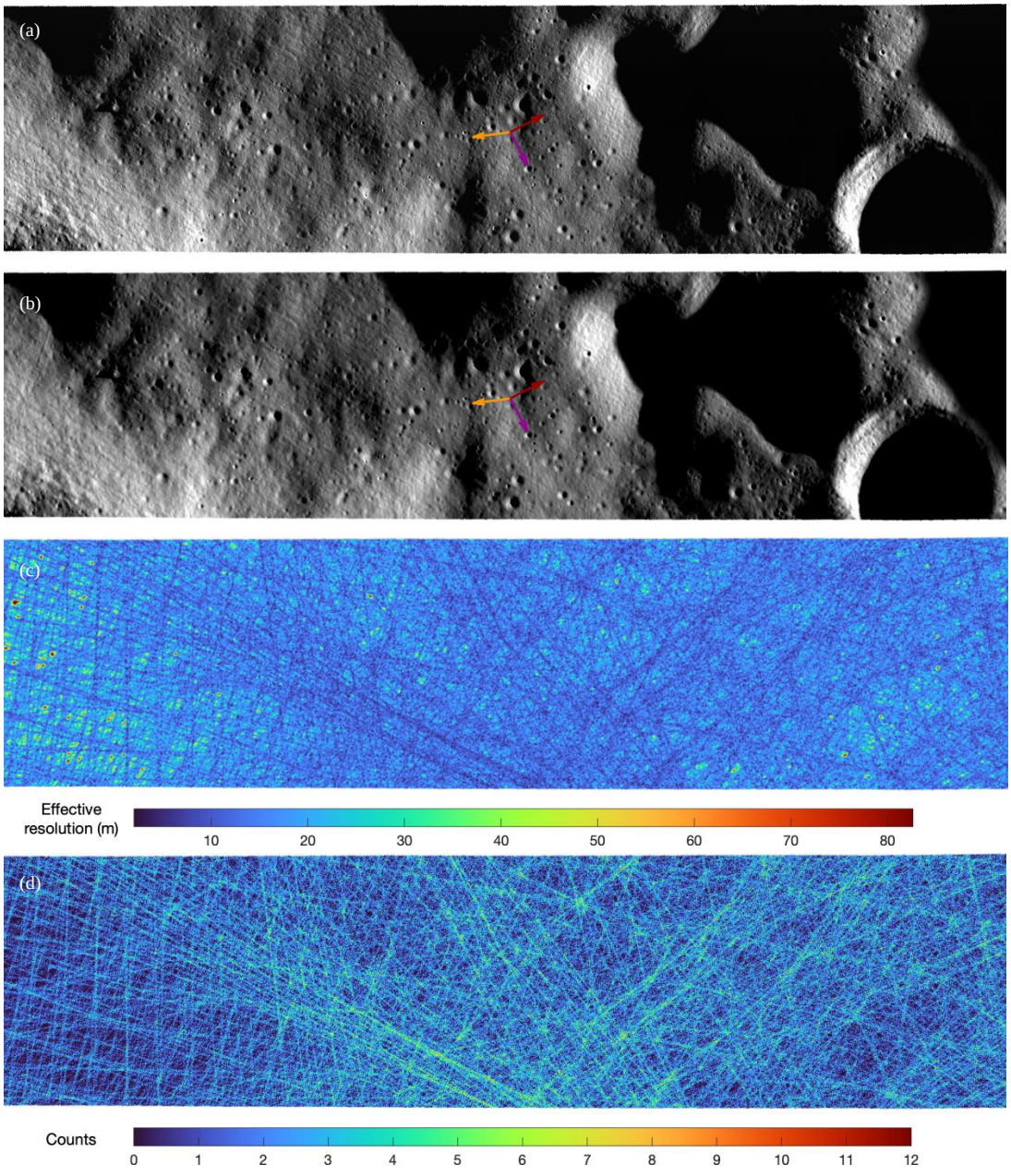

Figure 3 – (a) Sub-region of a 20 m/pix map-projected NAC image M139729686, (b) 20 m/pix rendered LDEM, (c) LDEM effective resolution in meters, (d) LDEM counts/pix. The **1 km**-long arrows indicate the direction to the south pole (orange) and stereographic +X/+Y (purple/brown).

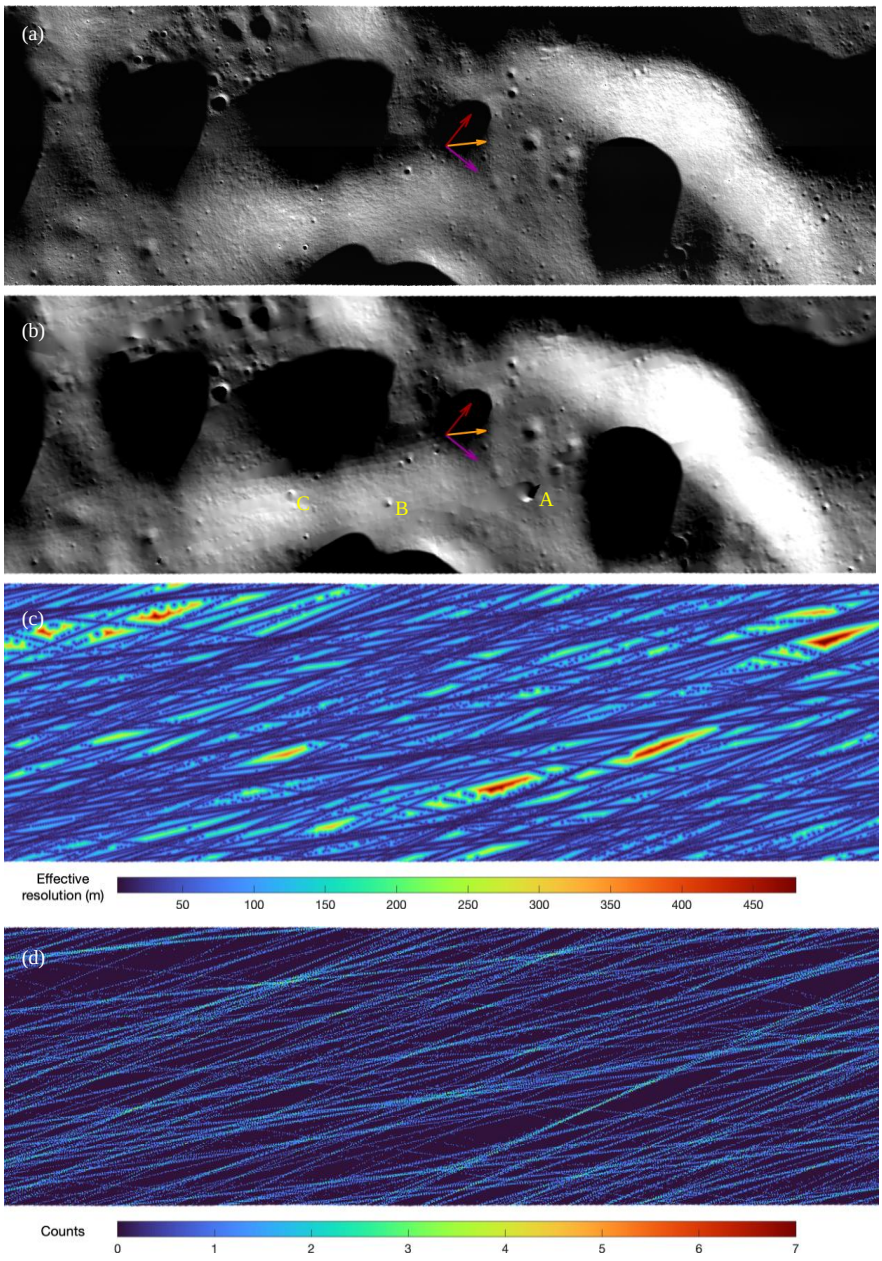

Figure 4 – Same as Figure 3, but for NAC image M151364517. Points labeled A – C are examples of likely spurious noise points.

Figure 5 shows the distribution of total offsets (summed over all iterations) in the along-

track/cross-track/radial (ACR) directions for all track segments. The RMS total ACR offsets were 8.7/9.5/0.64 m and the central 68th percentile widths were 7.4/7.6/0.34 m, which are consistent with the estimated LRO orbit reconstruction accuracy (Mazarico et al. 2018). The RMS cross-track offset is slightly higher than the along-track (median ACR offsets were 0.08/-1.8/0.04 m), which may be due to a small laser boresight (pointing) bias less than the width of the 5 m laser spot diameter.

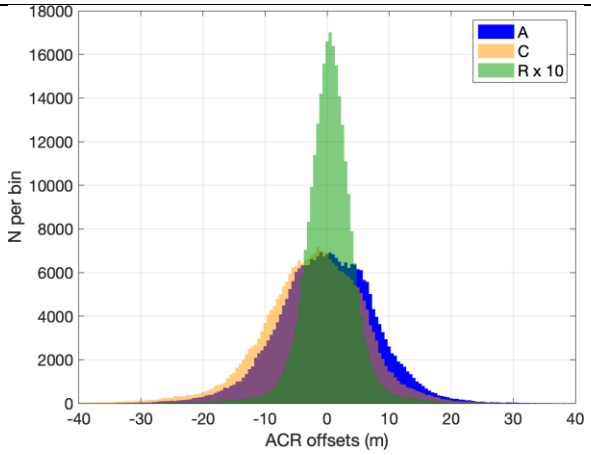

Figure 5 – Distribution of along-track/cross-track/radial (ACR) offsets for all track segments in 80° – 90° S. Note that the radial offsets have been scaled by a factor of 10 for clarity.

Poleward of 80°S there are ~1 million laser spot pairs with separations < 1 m. Figure 6 shows how the track adjustment process has improved their height differences as a function of slope derived from the 20 m/pix LDEM. The solid white lines are the median and inter-quartile range of the pairwise height differences before (left panel) and after (right panel) adjustment. Initially, their median height differences ranged from ~0.4 m at the lowest slopes to ~4 m at the highest slopes (left panel). After the track adjustment process, their height differences range from ~0.2 m at the lowest slopes to ~0.4 m at the highest slopes (right panel). We use a simplified model to approximate the spots' height differences as due to their physical separation as well as their range errors and geolocation errors while ignoring sub-footprint terrain roughness (see Supplementary Material for details). The model provides a good match to the initial median and interquartile range (left panel) with ACR geolocation errors of 7.00/7.00/0.40 m (dashed magenta lines). The model underpredicts the final median and interquartile range (right panel) when the geolocation errors are 0.00/0.00/0.00 m (dashed black lines) but overpredicts the data if the geolocation errors are 1.00/1.00/0.15 m (dashed red lines). The model does not explicitly account for sub-footprint terrain roughness, which could be contributing to the apparent final geolocation errors and slope trend in the right panel but would be negligible compared to the initial geolocation errors in the left panel. Therefore, we consider 1.00/1.00/0.15 m as a conservative estimate of the final track geolocation errors.

Thus, the final total geolocation uncertainty has been reduced by about an order of magnitude relative to the original geolocation uncertainties. This geolocation uncertainty applies to total absolute position rather than the uncertainty in a DEM pixel's surface height (i.e., elevation above the reference sphere), which we examine next.

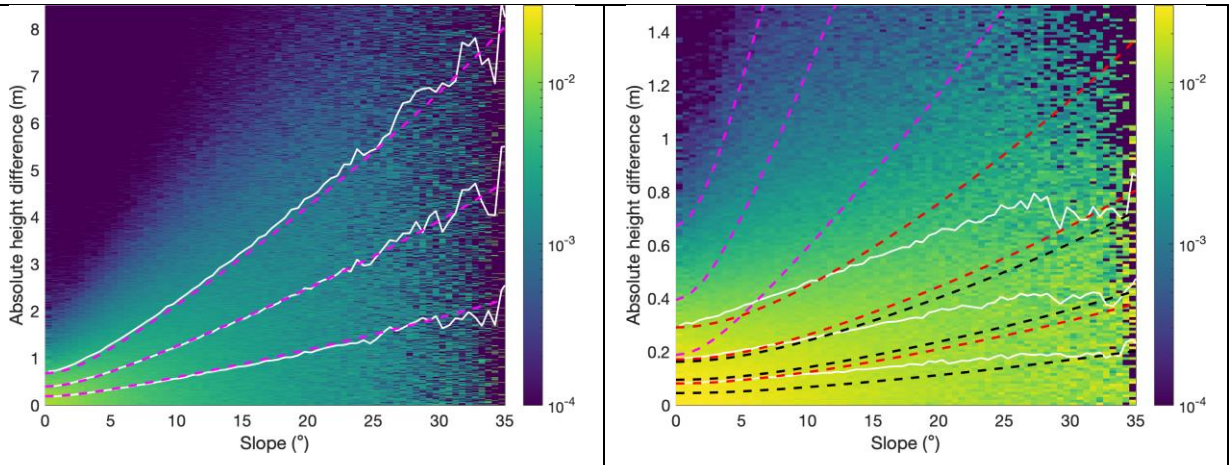

Figure 6 – Height differences of spots < 1 m apart poleward of 80°S before (left panel) and after (right panel) the track adjustment process (note the difference in vertical scale). Each panel is a 2-dimensional histogram with each column normalized by the total number of points in that column. The color scale gives the fraction of each column's total within each bin. The solid white lines are the median and inter-quartile range of each column. Dashed lines show a simplified model that ignores sub-footprint terrain roughness but has ACR geolocation errors of 7.00/7.00/0.40 m (magenta), 1.00/1.00/0.15 m (red), and 0.00/0.00/0.00 m (black).

In general, proper usage and interpretation of any DEM requires understanding its uncertainties, which can be difficult to quantify due to the vagaries of spacecraft and instrument behavior and unknown topography. Barker et al. (2021) made the first rigorous estimates of uncertainties in the cleaned 5 m/pix LDEMs using methods developed for the GRAIL gravity field (Lemoine et al. 2014) and we adopt the same method here. In summary, we avoid the infeasible computation of the LDEM's full error-covariance matrix, and instead generate an ensemble of 'clone' LDEMs with similar error properties as the nominal LDEM. Each clone is generated by, first, merging a high-pass-filtered random fractal terrain with the low-pass-filtered LDEM, then sampling that merged terrain at the LOLA point locations and perturbing them by the observational errors (range error, geolocation errors), and, finally, gridding and interpolating the perturbed LOLA points in the same manner as for the original LDEM. We refer the reader to Barker et al. (2021) for additional details. The ensemble of clones can then be analyzed to estimate quantities such as the RMS height error or the RMS slope error.

Given the large areas covered by the new LDEMs presented here, it is still computationally prohibitive to generate clones for all 64 tiles. Instead, we generate a set of clones for a representative subset of 4 tiles that sample the wide range of effective resolution, which is the primary factor influencing the uncertainty. A piecewise linear spline is then fitted to the RMS height and slope uncertainty as a function of effective resolution (Figure 7). The MAD of the spline fit residuals is typically ~20%. The fits are truncated at an effective resolution of 700 m as there are very few pixels beyond that, representing the 99.9999th percentile, and any pixels with a larger effective resolution are assigned an uncertainty corresponding to 700 m. Maps of effective resolution are then converted to RMS height and slope uncertainty using the spline fits (Figure 8). This is done for each LDEM pixel scale separately since the spline fits exhibit a modest dependence on pixel scale (more so for slope uncertainty than for height). These uncertainty maps represent the uncertainty in the LDEM gridded height and slope pixel values relative to the true average height and slope within each pixel.

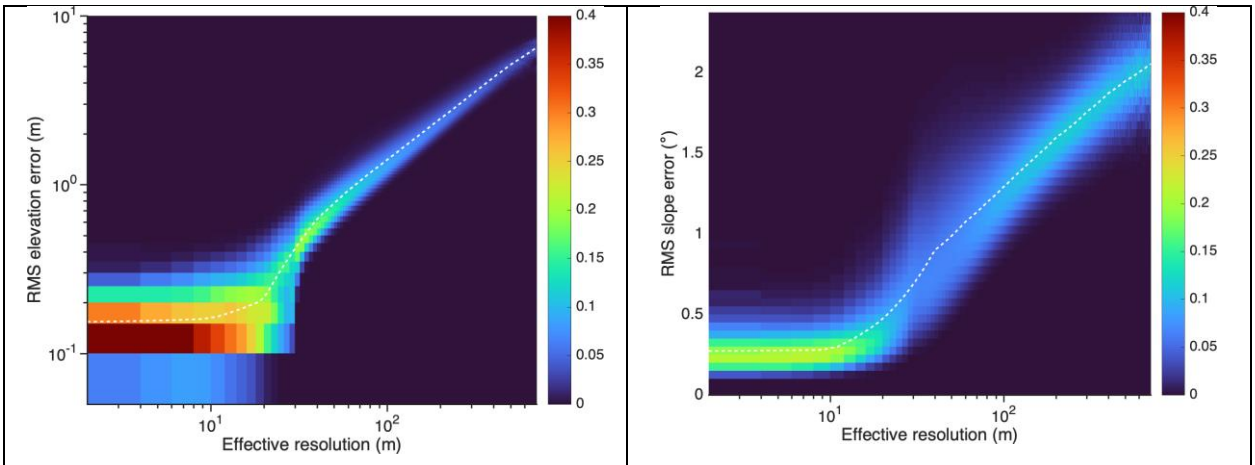

Figure 7 – RMS elevation error (left) and RMS slope error (right) as a function of effective resolution for a pixel scale of 20 m/pix. The color scale gives the fraction within a bin relative to the total within that bin's column. The dashed white lines are the piecewise linear spline fits.

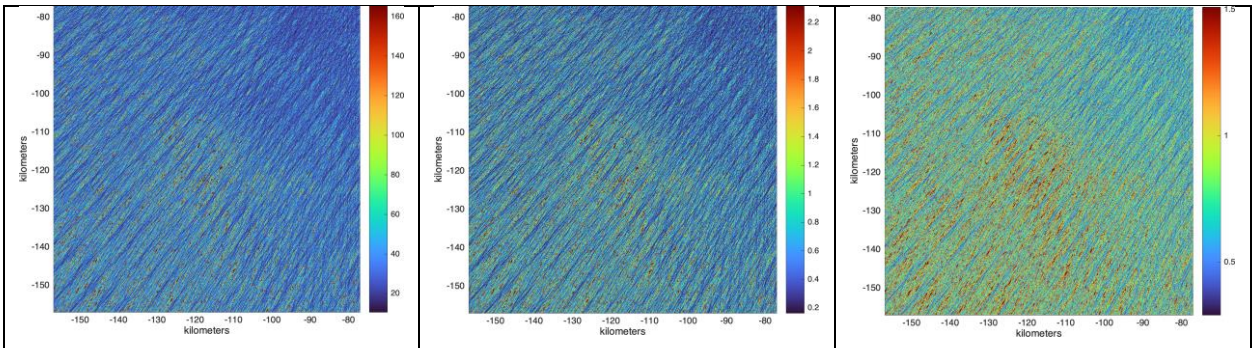

Figure 8 – Effective resolution in meters (left), RMS elevation uncertainty in meters (middle), and RMS

slope uncertainty in degrees (right) for the 80 km tile centered at (-114 km, -114 km) for a pixel scale of 20 m/pix. The color scale limits correspond to the 1st and 99th percentiles of each panel.

241

242

4 Roughness Maps

As explained in Section 1, terrain roughness is a useful probe of geologic processes on and below the surface over a wide range of time and spatial scales. It can also provide a wealth of information for landing site characterization locally and regionally. Therefore, we take a fresh look at the south polar regional roughness characteristics using the improved LOLA south polar altimetry and 20 m/pix LDEM. We made slope and roughness maps over a range of baselines (100, 200, 400, 800, and 1600 m) covering the 80° – 90° S region. Roughness was computed as a slope-detrended and outlier-resistant spread of height residuals. Specifically, every 50 m in stereographic X and Y, we fit a plane to the 20 m/pix LDEM sampled at 81 points uniformly distributed within a radius of half the baseline**.** Using the LDEM directly to fit the plane was found to be somewhat more stable to low numbers of LOLA spots compared to fitting the LOLA spots themselves. Then we compute the roughness as 1.48 times the median absolute deviation ($MAD_b = 1.48 \times MAD$) of height residuals of the individual LOLA spots within the same radius and relative to the plane. For normally-distributed data, MADb is equal to the standard deviation, but it is often favored over the latter due to its robustness to outliers and consistency as a scale estimator (Huber 1981; Leys et al. 2013).

Figures 9 and 10 show two examples of the resulting slope (of the best-fit plane) and roughness maps at baselines of 200 m and 1600 m (Figures A19 – A23 show the maps for all the baselines). Consistent with previous work (Rosenburg et al. 2011; Kreslavsky et al. 2013), the roughness generally increases with baseline in an absolute sense. Relative variations about this trend stand out when the maps are normalized to their own typical values, as in Figures 9 and 10. For example, the floors of Amundsen, Newton A, and Drygalski have relatively low roughness on a 1600 m baseline, but Amundsen and Newton A are relatively rougher than Drygalski on a 200 m baseline. Such differences can also occur outside large craters, as in the white boxes, A and B. Both boxes have relatively low roughness on a 1600 m baseline, but box A is rougher on a 200 m baseline. What causes these differences? Figure 11 shows a close-up of Box A. There is a pronounced increase in roughness at baselines < 400 m relative to 800 – 1600 m. This region is relatively heavily populated with craters of diameter < 400 m, which are too small to appear in the 1600 m slope and roughness maps and thus they are relatively smoother at the longest baseline.

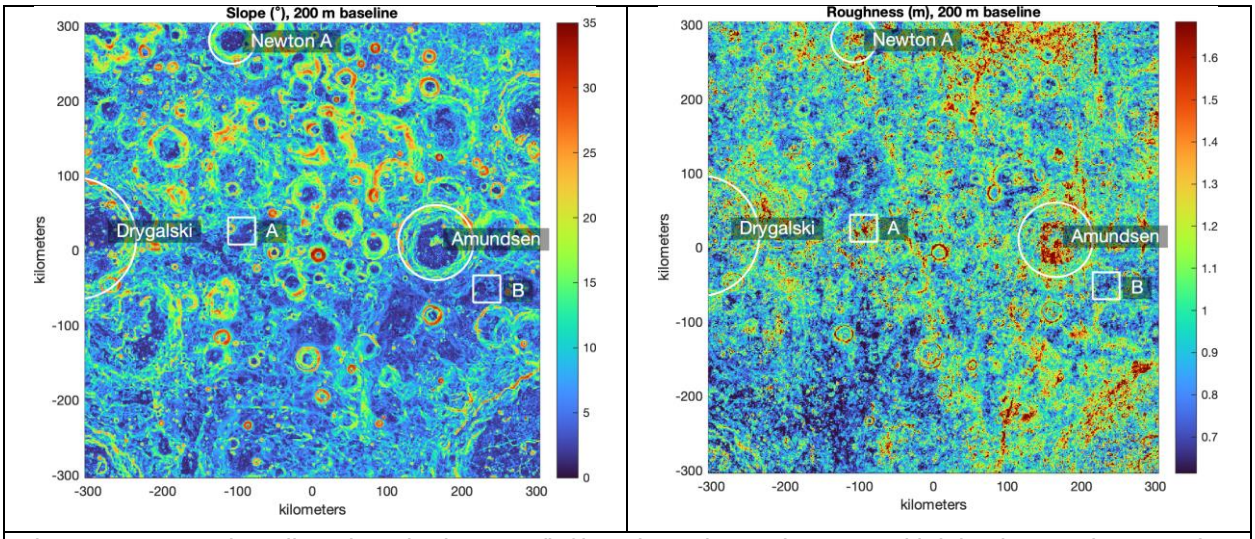

Figure 9 – 200 m-baseline slope in degrees (left) and roughness in meters (right). The roughness color scale ranges from the 2nd to the 98th percentile.

276

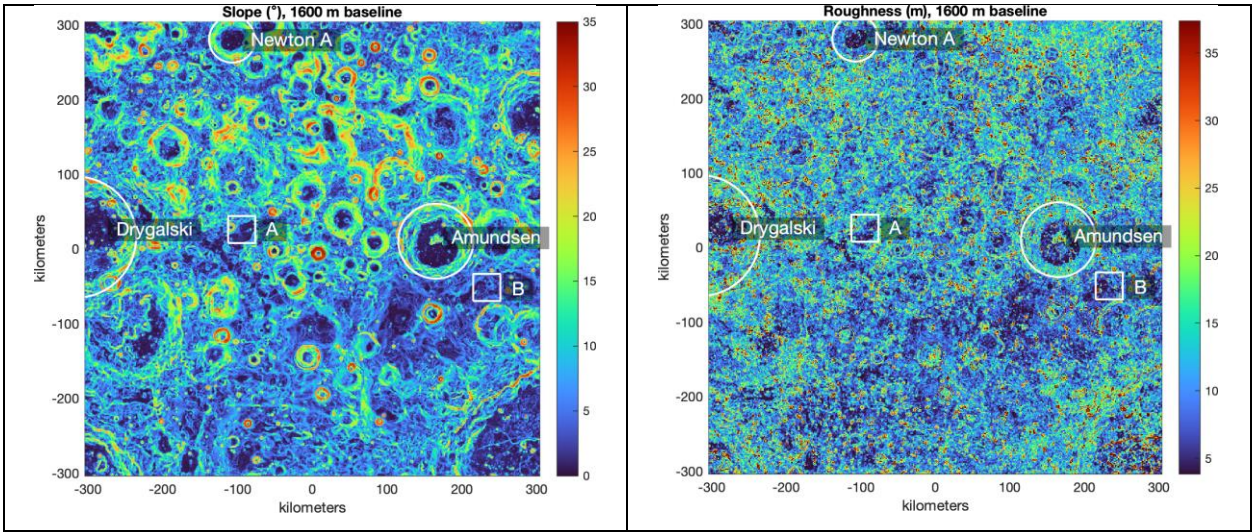

Figure 10 – Same as Figure 9, but for a 1600 m baseline.

277

278

279

280

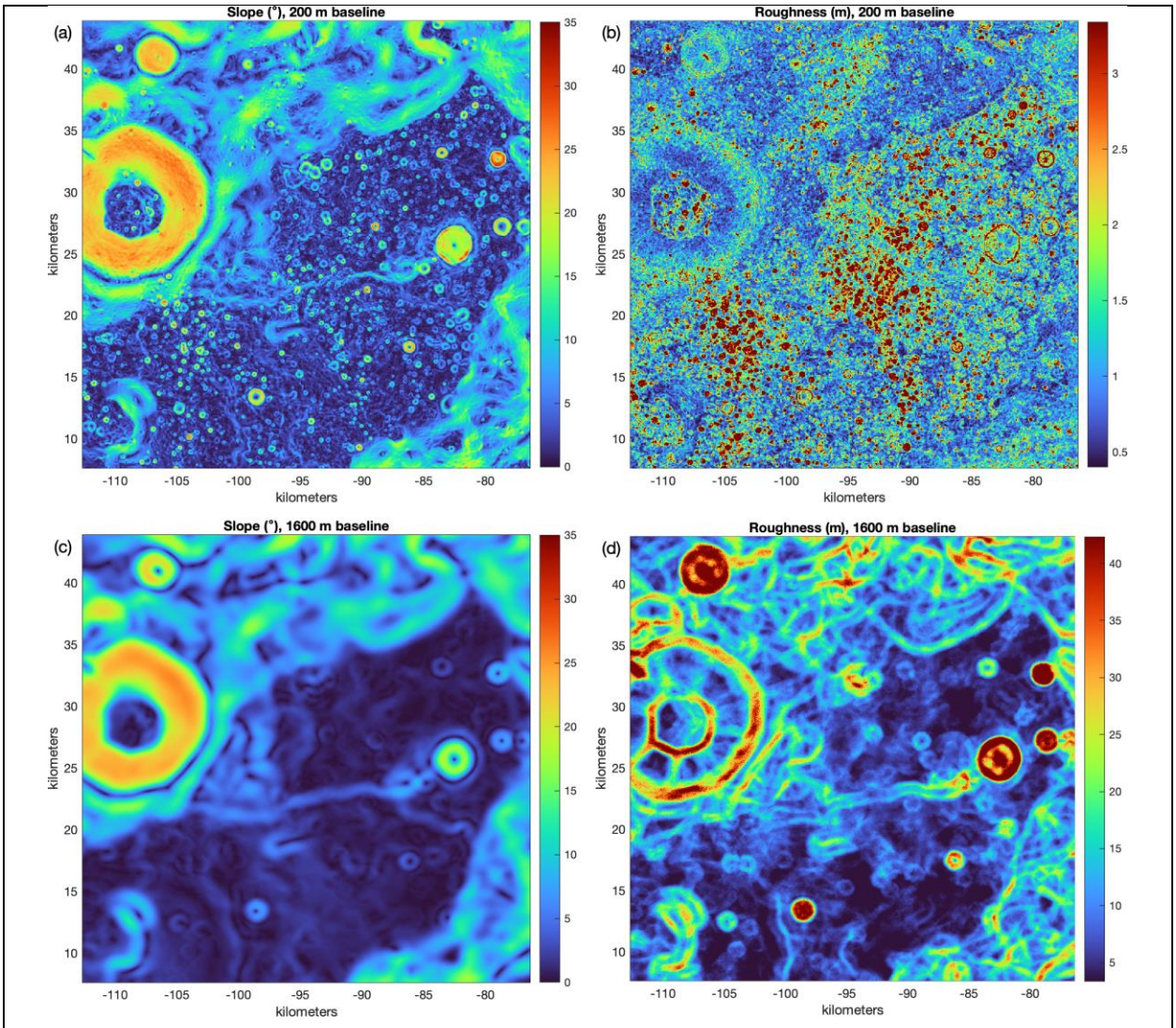

Figure 11 – Close-up of Box A in Figures 9 and 10 showing slope (left column) and roughness (right column) on 200 m (top) and 1600 m (bottom) baselines.

It can be helpful to visualize all the roughness maps as a single color-composite image as in Figure 12. In this figure, the roughness at each baseline is converted to a standardized value by subtracting the overall median and dividing by MAD_b. A strong intensity of a particular color signifies a high roughness at the corresponding baseline. In analogy with a reflectance spectrum, the slope of the "roughness spectrum" controls the overall color balance: cooler shades denote higher relative roughness on short baselines whereas warmer shades denote higher relative roughness on longer baselines. To extend our maps to smaller baselines, we supplement them with the LOLA single-shot roughness map already on the PDS (LDRM_40S_1000M_NN; http://imbrium.mit.edu/DATA/LOLA_GDR/), which is the

standard deviation of height residuals of LOLA's 50 m-wide 5-spot footprint relative to the footprint's best-fit plane (Neumann et al. 2015). This map, with an effective baseline of 50 m, has been used to study correlations between crater age, roughness, and cold-trapping ability (Deutsch et al. 2020).

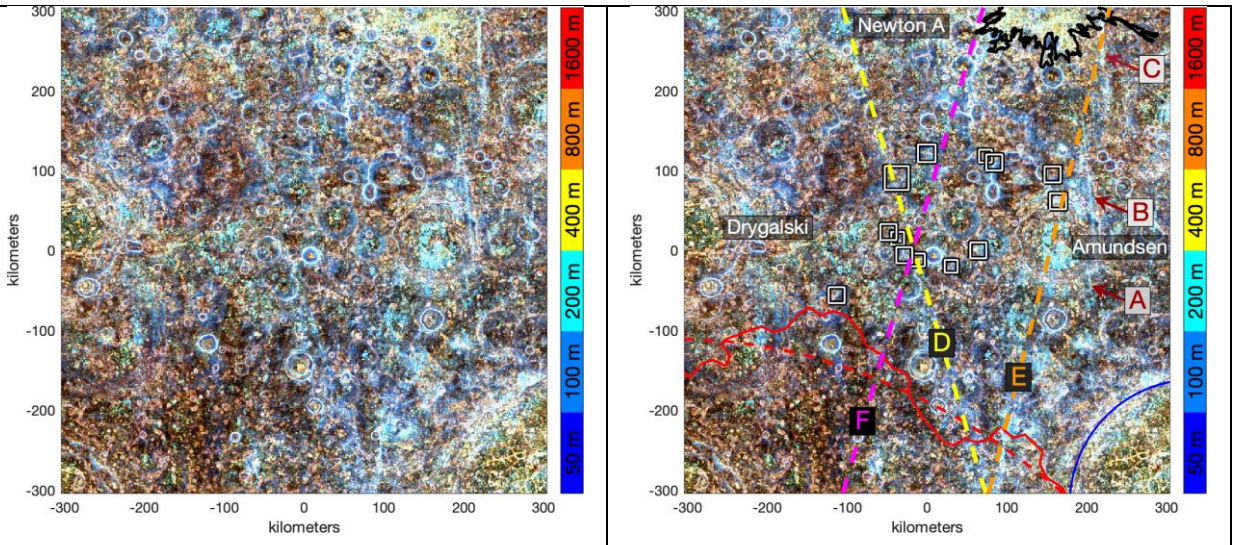

Figure 12 – Color composite image of LOLA roughness with each baseline assigned to a different color. White boxes are the current 13 Artemis III candidate regions.

Figure 12 reveals a diversity of terrains characterized by their roughness spectrum. For example, the Copernican-age Schomberger A ejecta blanket (black outline; Krasilnikov et al. 2023), whose topography is characterized by radial graben (Krasilnikov et al. 2023), is distinctly bright yellow in the roughness color composite. The South Pole-Aitken basin inner ring (dashed red curve; James et al. 2019) and Lunar Prospector FeO 7.7 wt% contour (solid red curve; Lawrence et al. 2002) correlate with a region of reduced roughness on short baselines. Some areas, such as the floors of Amundsen and Newton A, appear blue/cyan signifying, as discussed above, a pronounced increase in roughness at baselines < 400 m relative to 800 – 1600 m due to an excess number of craters of diameter < 400 m. Indeed, the floor of Newton A may be filled with secondary craters from a Tycho ejecta ray known to cross the south polar region (Wells et al. 2010; Lemelin et al. 2016b; Denevi & Robinson 2020; Bernhardt et al. 2022). The floor of Schrödinger exhibits predominantly red to yellow shades with topography characterized by mare-like volcanic plains and optically brighter smooth crater floor deposits cross-cut by graben of volcanic and/or tectonic origin (Kramer et al., 2013; Wilson and Head, 2018; Krasilnikov et al. 2023). Schrödinger's rim (solid blue line) appears strikingly different from its floor with a mix of all colors suggesting a variety of baselines dominating the roughness spectrum of the ejecta deposit on the rim.

Several linear features (A – C in Figure 12) may be examples of the roughness rays and

lineaments previously identified at lower latitudes in global hectometer-scale roughness maps and which may be chains of secondary craters (Kreslavsky et al. 2013). There is also tentative evidence for two additional diffuse, longer, and wider swaths (D and E) of variably high roughness on short baselines. Great circles through these features (dashed lines) also pass close to linear features equatorward of 80° S in maps of LOLA 50 m single-shot roughness, LOLA 1064-nm normal albedo, and LRO Wide Angle Camera (WAC) ultraviolet reflectance (Figure 13). Swath D is likely to be part of the Tycho ejecta ray (dashed yellow line in Figures 12 and 13) that passes through Newton A. Swath E (dashed orange line) passes close to several large craters (Antoniadi, Crookes, and Jackson) north of 80° S. Another linear feature (F) appears nearby and parallel to E perhaps originating in the same impact as E or with De Forest. However, there is no clear signal of F in the roughness maps poleward of 80° S.

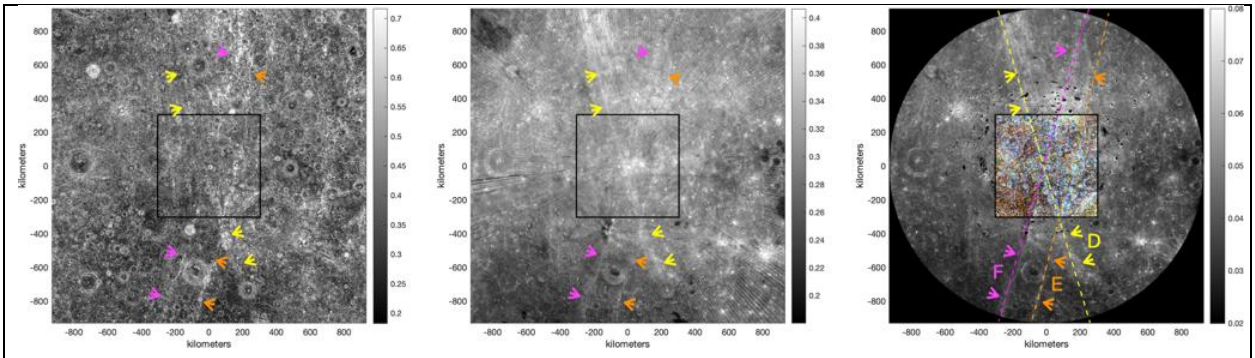

Figure 13 – LOLA roughness (meters) on 50 m baselines (left panel), LOLA 1064-nm normal albedo (middle panel), and LROC WAC 321 nm reflectance (right panel; Lunar QuickMap; https://quickmap.lroc.asu.edu/). The black square outlines the 80° – 90° S region covered by the color composite image (Figure 12), which is overlaid on the right panel where the WAC mosaic has no data. Candidate ejecta rays are labeled with arrows and, in the right panel, overlain with great circles.

If swath E is another ejecta ray, then that could explain why Amundsen's floor is so rough (~90th percentile) at short (≤ 400 m) baselines compared to other large craters, like Shoemaker, Schrödinger, and Drygalski. The large flat floors of these craters are relatively immune to the crater-erasing effects of downslope mass movement, but only Amundsen experienced the bombardment of secondary impactors responsible for swath E. Non-uniformities in swath width and roughness could reflect variations in secondary impactor properties (e.g., size, mass density, spatial density) and/or target terrain properties, notably slope leading to downslope transport and surface modification. Altogether, this view of the south polar region highlights the role that even far-away impacts have had in shaping the terrain including potentially within some Artemis III candidate regions. Therefore, such extended ejecta distributions should be considered when characterizing future landing sites and when interpreting sample provenance and

other in-situ/orbital data. The distribution of ejecta from these impacts can be mapped, in part, by LOLA topographic roughness.

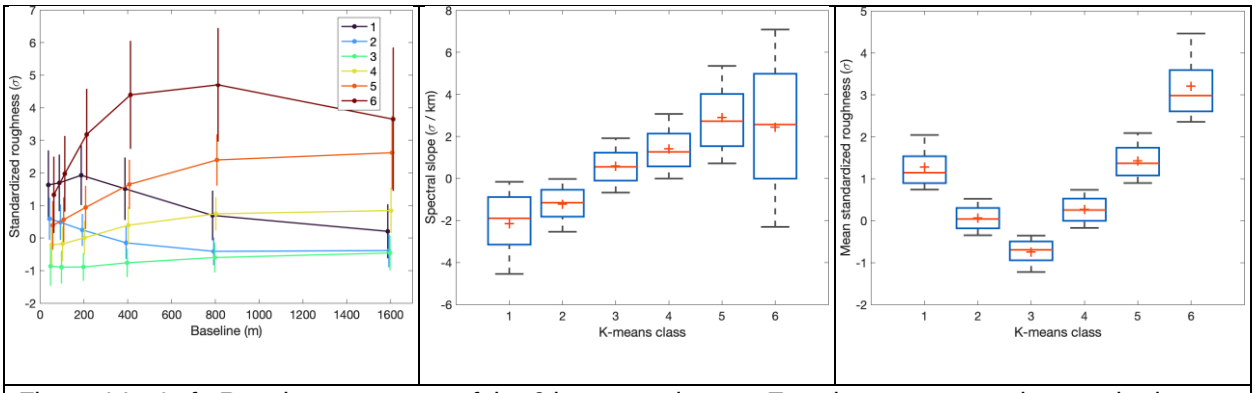

Figure 14 – Left: Roughness spectra of the 6 k-means classes. Error bars represent the standard deviation of 1 km pixels for each class and baseline. Middle: Box plots of the roughness spectral slope of the classes. Each box shows the median (horizontal line), mean (plus symbol), interquartile range (box edges), and 9th/91st percentiles (whiskers). Right: Box plots of the mean roughness over all baselines.

To further quantify the roughness characteristics in the polar region, we use the k-means algorithm (Loyd 1982) to classify map pixels according to their roughness spectrum. The k-means algorithm groups data into classes by minimizing the variance between all members of each class. The number of classes is a free parameter, which we set to 6 after trying values between 1 and 30. A value of 6 is large enough to capture the major geologic trends while small enough to keep the classes easily distinguishable.

Figure 14 (left panel) shows the resulting average roughness spectra of the 6 k-means classes numbered and colored from cold to hot in order of increasing overall spectral slope (middle panel). As previously discussed, the roughness spectral slope controls the color balance in the composite image, Figure 12. Indeed, the map of k-means classes (Figure 15) shows that the spatial locations and relative spectral slopes of the classes have a good correspondence with the color composite (Figure 12). The most common class is 3 with a relatively flat, slightly positive roughness spectrum and the lowest mean overall roughness (Figure 14, right panel) owing mostly to diminished roughness on < 800 m baselines which causes this class to appear red to yellow in Figure 12. Crater rims and massif ridges tend to be class 5 or 6. Crater walls and massif sides tend to be class 1 or 2 unless they are part of very large and degraded craters (e.g., Amundsen, Schrödinger, Drygalski). The linear features and swaths also tend to be class 1 or 2 with the lowest spectral slopes and bluest colors in the color composite (Figure 12). There is a trend of increasing mean roughness with increasing spectral slope in classes 3 – 5, less so for 6

(Figure 14, right panel). Extrapolating this trend to classes 1 and 2 would underpredict their overall mean roughness due to their excess roughness at small baselines. Classes 3 – 6 are more easily distinguished by mean roughness than by spectral slope, but had we run the k-means algorithm on mean roughness, it would have mixed classes 1 and 2 with the others.

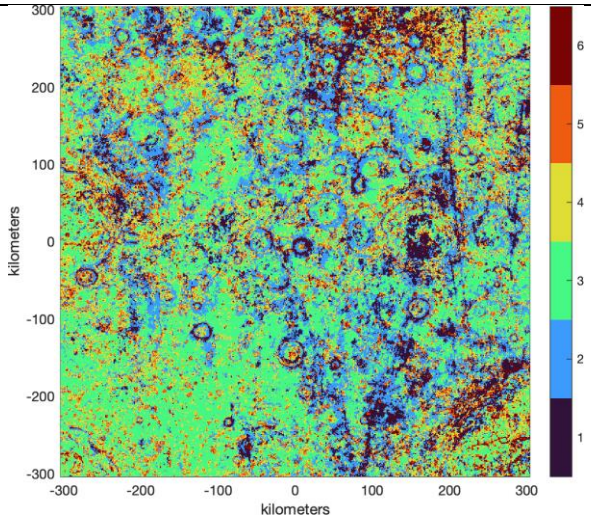

Figure 15 – 1 km/pix map of the k-means classes with cold to hot colors representing low to high roughness spectral slope.

The k-means classes show weak, but suggestive correlations (Figures 16 and Figures A24 – A26) with the LOLA 1064-nm normal albedo and composition (e.g., FeO) from the Kaguya Spectral Profiler maps of Lemelin et al. (2022). However, the classes do not correlate with optical maturity (OMAT) or nanophase iron abundance (Figure A25) from those same maps. This behavior does not significantly change when controlling for topographic slope. But, controlling for 1064-nm normal albedo does remove the compositional trend suggesting a real trend in the reflectance spectra of the classes. If cratering is the primary driver of the roughness we are measuring, then this could mean that, on average, in this region, the excavated material has lower FeO and similar OMAT as the background terrain. Lemelin et al. (2022) noted a general increase in OMAT towards the poles possibly due to reduced solar wind flux. This could reduce the OMAT contrast between freshly excavated material and the background terrain making it harder to distinguish subtle OMAT variations between the classes. Also, we note that the difference in FeO between the k-means classes is less than the ~ 1 wt.% uncertainty of the FeO values themselves (Lemelin et al. 2022). The more directly observable quantity, normal albedo, is not subject to the modeling uncertainties in FeO and OMAT. Therefore, it cannot be ruled out that the albedo trend exhibited by the classes is entirely due to exposure age rather than composition. In this scenario, more heavily cratered terrain has a higher roughness and higher albedo because the crater walls are continuously replenished

with fresh material due to mass wasting and the ejecta of young craters may still be optically immature.

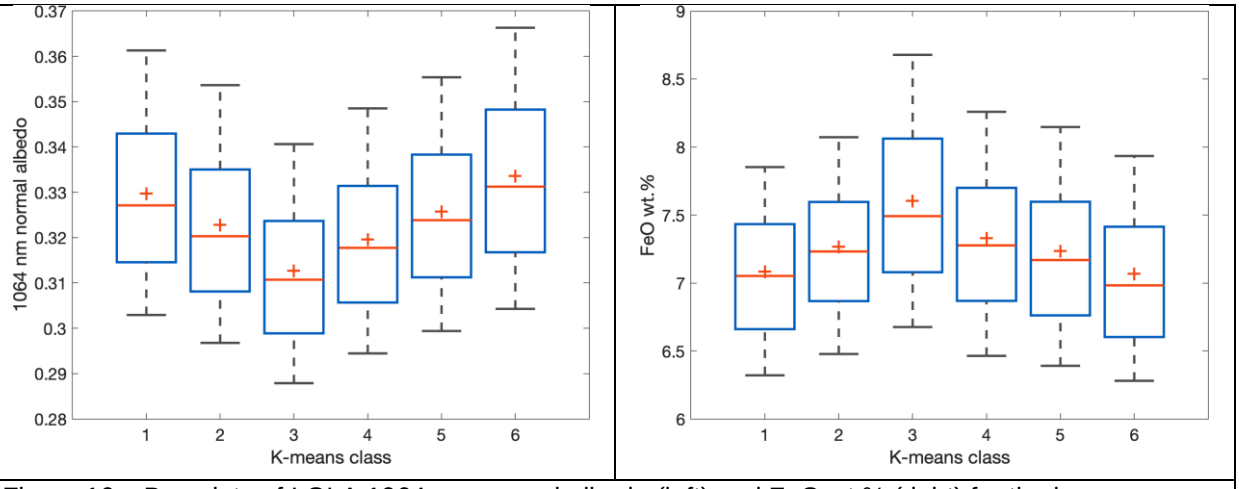

Figure 16 – Box plots of LOLA 1064-nm normal albedo (left) and FeO wt.% (right) for the k-means classes. Each box shows the median (horizontal line), mean (plus symbol), interquartile range (box edges), and 9th/91st percentiles (whiskers).

As discussed above, an excess number of craters on baselines < 400 m leads to a more negative roughness spectral slope and bluer shades in the color composite (Figure 12). However, downslope mass transport processes are known to quickly erase craters on even gentle topographic slopes (≳5°; Xiao et al. 2013; Basilevsky et al. 2019; Zharkova et al. 2020). Therefore, the topographic roughness on all but the flattest terrain is likely to be heavily dependent on these mass transport processes. Indeed, the relative frequency of classes is correlated with topographic slope (Figure 17) and vice-versa (Figure A27). In Figure 17, the typical class designation changes from 2 to 3 going from slopes of ~0° to ~5°, and then gradually declines to 1 at the highest slopes. A similar trend holds for spectral slope within each class. This trend may be due to downslope mass transport processes efficiently erasing the cratering roughness signature in favor of a background regolith textural signature whose short-baseline roughness increases with slope. This regolith textural component may be related to the “elephant hide” texture that is ubiquitous on sloped terrain (Zharkova et al. 2020; Kreslavsky et al. 2021). NAC images confirm that low-topographic-slope class 1 tends to be significantly more heavily cratered than high-topographic-slope class 1 with only the latter exhibiting the elephant hide texture (Figures A28 – A30).

As an additional test, we generated an alternative k-means classification scheme directly incorporating topographic slope. This alternative classification had seven classes and included the 1600-m baseline slope as a seventh datatype (in addition to the six roughness baselines as before). Most of the resulting new classes were strongly correlated with topographic slope over the full range of slope values

(Figure A31). In the new classification, low-topographic-slope terrain was divided into two separate classes with a relative proportion of approximately 70%/30%. The higher-percentage class belonged to the topographic slope-dominated roughness trend which we interpret as due to downslope surface modification. The lower-percentage class exhibited a mean roughness spectrum similar to the original class 1 in Figure 14 (i.e., a high overall roughness and an excess roughness on 200 – 800 m baselines), which we interpret as due to the secondary crater population. It is possible that instrumental effects such as degrading range precision with increasing slope could contribute to the slope trend. However, given that the NAC images apparently show qualitatively genuine differences between the k-means classes, we think that the slope trend is primarily a real effect.

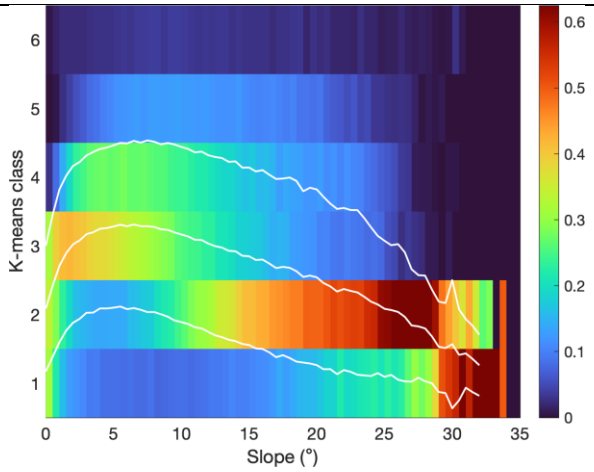

Figure 17 – 2-D histogram showing the relative frequency of the k-means classes as a function of 1600 m-baseline slope. Each column is normalized to the total number of points in that column with the color indicating the fraction of each column's total within each bin. The white lines show the mean and standard deviation.

Additional insight on topographic roughness comes from the deviogram of topography, which describes the behavior of RMS height deviations as a function of baseline. The slope of the deviogram on a log-log plot is referred to as the Hurst exponent, H. Fractal topography has an H = 1.0. On the Moon, H has been measured to be close to 1 in the highlands and maria on baselines of meters to tens of meters (Cai & Fa 2020). On larger scales (~50 m to several km), the median H in the highlands and south pole is 0.95 while in the maria it is 0.76 (Rosenburg et al. 2011). Here we study the Hurst exponent of the south pole at higher resolution by sampling the 20 m/pix LDEM at the same 50-m grid points as for the roughness maps. We compute the RMS height deviation (RMSd) between each grid point and a series of

concentric annuli with diameters given by the same baselines as above. The resulting map of Hurst exponent fitted to baselines of 100, 200, 400, and 800 m, downsampled to 1 km/pix, has a median and interquartile range of 0.98 and 0.94 – 0.99, respectively (Figure 18). Terrain characterized by low 1600 m-baseline slopes (~0° – 4°) tends to have smaller H (~0.6 – 1.0) than terrain with higher slopes where H is predominantly close to 1.0. This is qualitatively consistent with the dependence of roughness spectral class/slope on topographic slope discussed above. Class 1 has the largest spread in H values reflecting its wide range of topographic slopes and the predominance of craters in this class much smaller than the largest baseline fitted (further explained below).

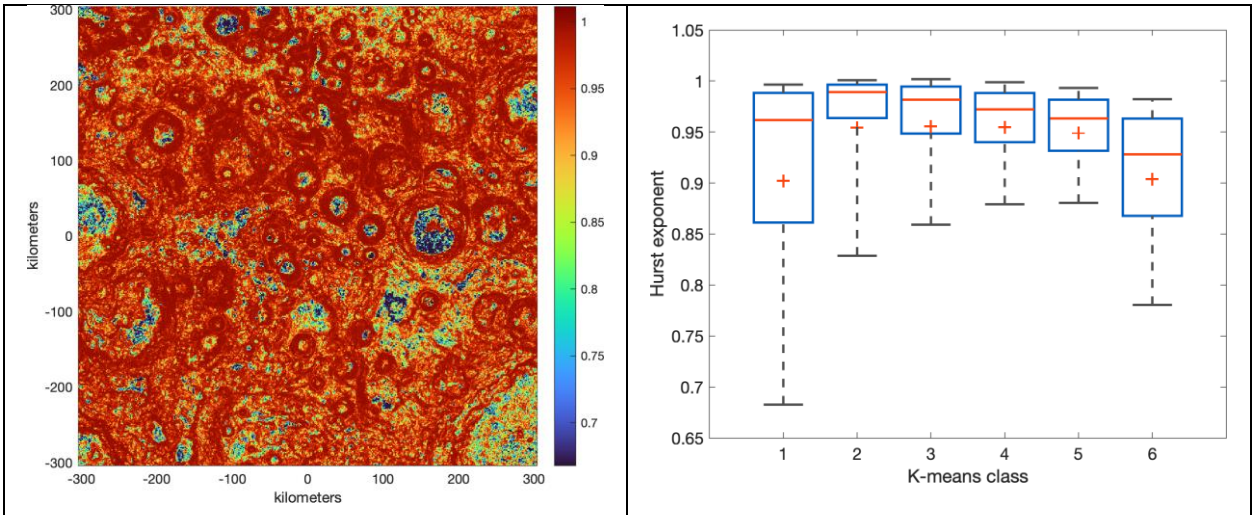

Figure 18 – Left: Hurst exponent over 100 – 800 m baselines (1 km/pix). The color scale ranges from the 2nd to the 98th percentile. Right: Same as Figure 16, but for the Hurst exponent of the k-means classes.

The Hurst exponent can also be isolated to different baseline ranges by taking the ratio of different RMSd maps (Figure 19b and 19e). From Figure 19, we see that the Hurst exponent is generally smaller at 800 – 1600 m baselines than at shorter baselines. This is consistent with the common flattening of deviogram shapes measured globally in the highlands for baselines larger than ~ 1 km (Rosenburg et al. 2011). However, we find that this effect is most pronounced over terrain that is relatively flat at the 1600 m baseline and where smaller, hectometer-scale craters are common. We attribute this effect to the fact that the Hurst exponent measured inside individual craters depends on their size relative to the baseline. Figure 19 shows that the walls of craters much larger than the baseline have H ~ 1 while their flatter, more heavily cratered floors tend to have lower H. As crater size relative to the baseline decreases, H on both the walls and floors decreases. Hence, terrain dominated by craters smaller than the baseline tends to have lower H compared to less cratered terrain.

445
446

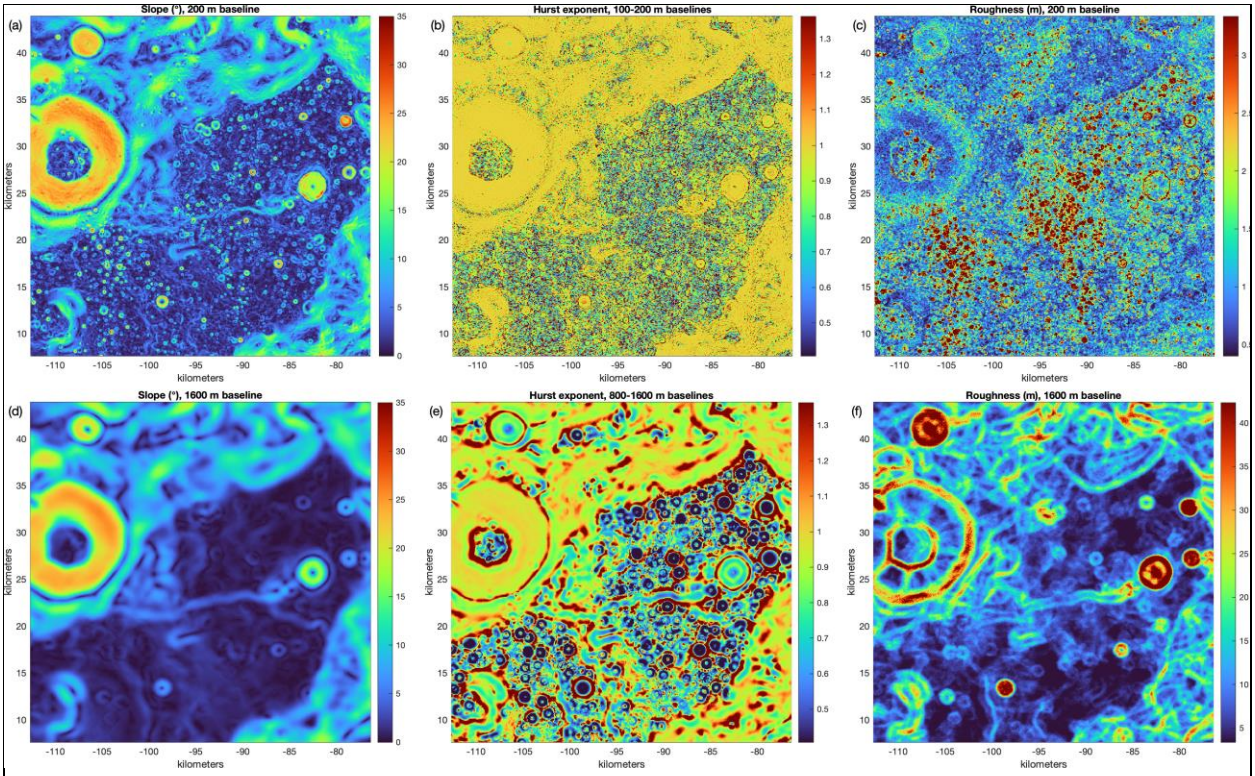

Figure 19 – Comparison between slope, Hurst exponent, and roughness on 200 m (upper row) and 1600 m (lower row) baselines at 50 m/pix. The Hurst exponent is generally smaller at 800 – 1600 m baselines (e) compared to 100 – 200 m baselines (b), and the Hurst exponent inside individual craters decreases as their size relative to the baseline decreases.

447
448

5 New PSR map

Micro cold traps with sizes of ~1 – 10 cm were predicted to be the most numerous and contribute ~10 – 20% of the total cold trap area on the Moon (Hayne et al. 2021). Such small micro cold traps are not resolvable with past or current orbiting instruments. However, larger cold traps with sizes of order ~10 – 100 m are more readily identified with extant datasets, such as the new LOLA 20 m/pix DEM. This product allows for the derivation of a new PSR map that is both cleaner and higher-resolution than the current PSR map (60 m/pix) archived on the PDS.

The angular elevation of the local horizon is computed in all directions for every pixel using a series of nested maps with progressively lower resolution to cover increasingly larger horizon distances starting with 20 m/pix out to a distance of 7 km and ending with 480 m/pix at a distance of 310 km. The next step involves computing the illumination conditions at hourly timesteps over the full lunar precession cycle of 18.6 years at 20 m/pix, a task which is computationally prohibitive. However, all we need to make the PSR map is to simulate the maximum illumination times at the south pole. We do this by creating a fake kernel in the SPICE toolkit (Acton 1996; Acton et al. 2017) that places the Sun on the celestial sphere at the minimum declination that it ever experiences over 18.6 years. That allows a simulation of southern summer in just 720 timesteps instead of the 165,000 that were previously necessary.

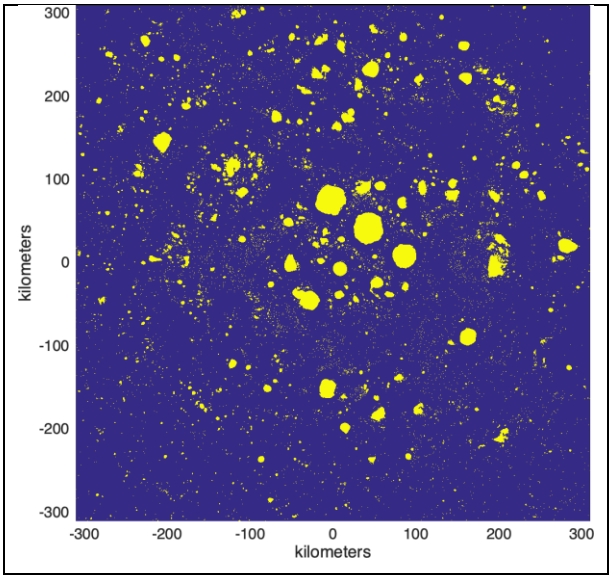

Figure 20 – New 20 m/pix map of PSRs within 80° – 90° S.

Figure 20 shows the new 20 m/pix south polar PSR map. There are 506,349 individual PSRs

(groups of pixels connected at the sides or corners) with an area ≥ 1 pixel contained within the total map extent, 466,204 of which lie poleward of 80° S (i.e., excluding the corners of the map). The cumulative size-frequency distribution (CSFD) shows an approximately power-law behavior with spatial variation (Figure 21, left panel). Fitting a power law to PSR areas < 10 km^2 within 9 equal-area annuli centered on the pole (the annulus width decreases with distance from the pole) gives a mean exponent of -0.77 ± 0.07 with little dependence on the exact lower limit of PSR areas fitted. Therefore, most of the spatial variation in the power law exponent is likely real rather than due to the varying CSFD completeness (further details below).

The largest PSRs contribute the most to the total PSR area. Despite their larger numbers, smaller PSRs contribute progressively less to the cumulative area-frequency distribution (CAFD; Figure 21, right panel). Poleward of 80° S, the total PSR area is 20,800 km^2 for individual PSR areas of at least one pixel or 20,600 for PSR areas ≥ 5 pixels, in good agreement with the value 20,900 found by O'Brien & Byrne (2022) using the old 30 m/pix map and a horizon-based illumination algorithm. Defining PSR "size" as the diameter of a circle with the same area, PSRs with sizes of 22 m (1 pixel) to 1 km (1963 pixels) contain, on average, 15% ± 5% of the total PSR area within each of the 9 concentric annuli.

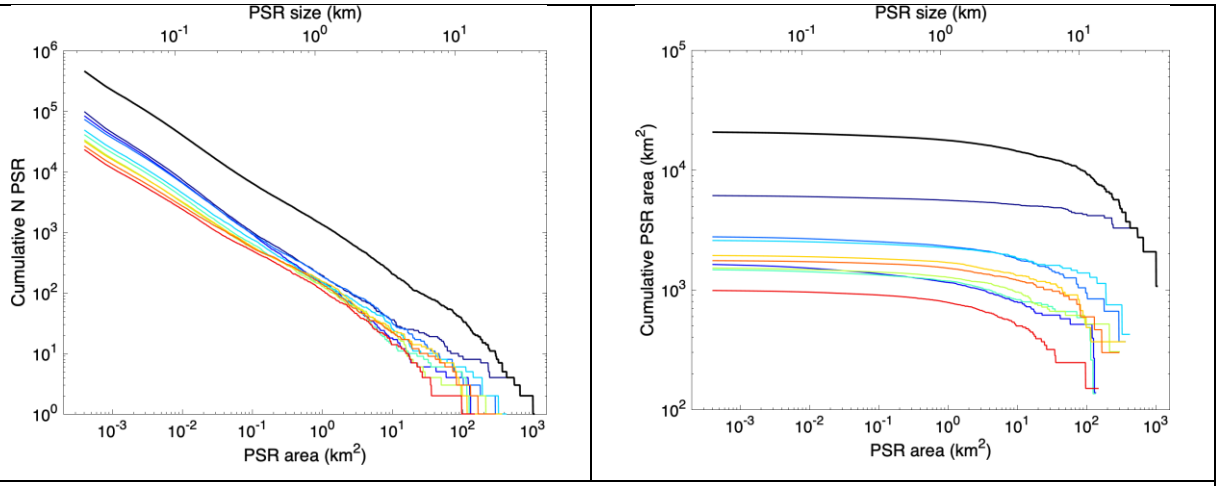

Figure 21 – PSR cumulative size-frequency distribution (left) and cumulative area-frequency distribution (right) for 80° – 90° S. In each panel, the total distribution (thick black line) is compared to that in 9 equal-area annuli moving out from the pole (dark blue to red thin lines) with outer radii of 101.33, 143.31, 175.51, 202.67, 226.59, 248.21, 268.10, 286.61, and 304.00 km.

When interpreting the LOLA PSR map it is important to understand that some pixels may be false positives or false negatives due to gaps between laser spots and to imperfections in the LDEM surface (although the latter has been minimized in the improved maps derived here). These effects can cause the measured CSFD and the sizes of individual PSRs to differ from the true ones. We study these effects

using the clones of the tiles that were used in Sec. 3 to derive uncertainties. That section described the clone generating process. The only additional step here involves computing the PSR map (using the same method described above) for two individual clones, one for the innermost tile, centered at (-39, -39) km or (88.1813° S, 225.0000° E), and one for the outermost tile, centered at (-273, -273) km or (77.3199° S, 225.0000° E). Figure 22 shows that the recovered PSR CSFD is generally lower than the true one at small PSR sizes. All else being equal, the completeness rate decreases as PSR size decreases because smaller PSRs are more likely to lie in gaps between LOLA spots. Since the LOLA spot density decreases (effective resolution worsens) with distance from the pole, the PSR CSFD completeness rate also decreases farther from the pole.

For the innermost tile (Figure 22, right panel), the median effective resolution is 20 m, and the CSFD is ~70% complete down to the smallest PSR area of 1 pixel (4×10^{-4} km^2 or 22 m in size), ~75% complete for PSR areas ≥ 4 pixels (1.6×10^{-3} km^2 or 45 m), and ~90% complete for areas ≥ 20 pixels (8×10^{-3} km^2 or 100 m). For the outermost tile (Figure 22, left panel), the median effective resolution is 56 m, and the CSFD is ~40% complete for areas ≥ 1 pixel, ~75% complete for areas ≥ 20 pixels, and ~90% complete for areas ≥ 78 pixels (3.12×10^{-2} km^2 or 200 m). Incompleteness has a relatively small effect on the CAFD since smaller PSRs contribute progressively less to that function. For example, the total PSR area is 97% complete in the outermost tile.

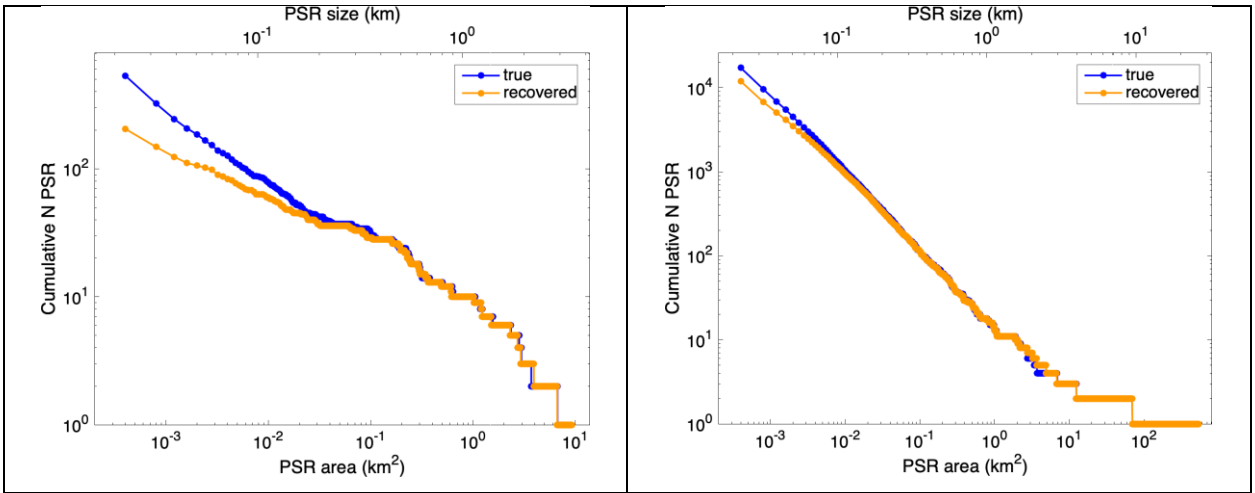

Figure 22 – Cumulative size-frequency distributions (CSFDs) of PSRs for two simulated clones of the 80x80 km tiles centered at (-273, -273) km (left) and (-39, -39) km (right). Each point represents an increment of 1 pixel (4×10^{-4} km^2) in PSR area. Gaps between LOLA laser spots increase in size and number moving farther from the pole causing the recovered CSFD (orange) to be progressively lower than the true CSFD (blue) farther from the pole. All else being equal, the completeness rate decreases as PSR size decreases because smaller PSRs are more likely to lie in gaps between LOLA spots.

The PSR completeness rate does not tell us about the accuracy of the recovered PSR areas. To answer this question, we find the closest true PSR to every recovered PSR and compute the fractional error in recovered area. We show this fractional area error for all PSRs in both tiles in Figure 23. In this figure, the blue points' x and y values (PSR area and PSR area fractional error) are discretized because PSRs can only be an integer number of pixels. For example, recovered PSRs 1 pixel in area (corresponding to the first column of points at 4×10^{-4} km^2) can only be in error by 0.0, -0.5, -0.67, …, -1/N if the true area is 1, 2, 3, …, N pixels, respectively. Evidently, PSRs 2 pixels in area (8×10^{-4} km^2) are never overestimates of 1-pixel PSRs, but PSR areas of 3 or more pixels can be over- or underestimates. However, most recovered PSR areas tend to be underestimates of the true areas likely due to the incomplete sampling of the surface inherent in the LOLA spot distribution. The behavior does not drastically change with effective resolution, as the outermost tile has only a somewhat lower accuracy of the recovered areas by ~ 0.1 – 0.2 for PSR sizes < 200 m. For larger sizes, the fractional error magnitude is typically < 0.1 regardless of effective resolution. The behavior also does not significantly change if we enforce a distance criterion on the matches between true and recovered PSRs.

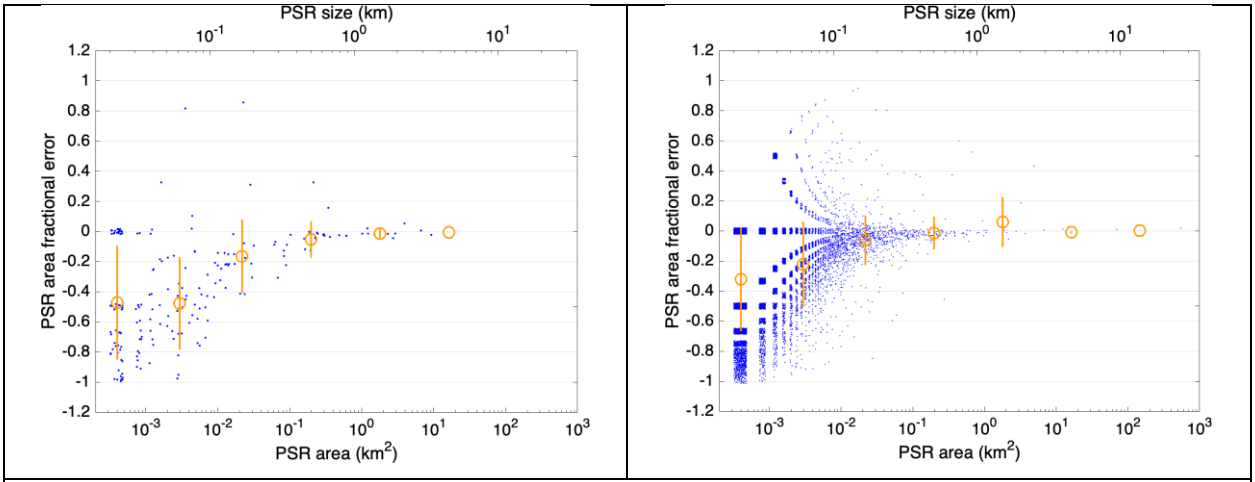

Figure 23 – Fractional error in recovered PSR area for two simulated clones of the 80x80 km tiles centered at (-273, -273) km (left) and (-39, -39) km (right). Fractional error is defined in the sense of (recovered area – true area) / true area. The x-axis is the recovered PSR area. Blue points are individual PSRs with a small random offset added in x and y to show point density more clearly. Orange circles with error bars denote the mean and standard deviation.

Next, we examine the false positive rate, or the likelihood that any particular PSR pixel is not actually permanently shadowed. This could depend on the size of the PSR to which the pixel belongs (e.g., lower false positive rate within larger PSRs) and where in that PSR the pixel resides (higher false positive rate closer to the PSR's edges). For each recovered PSR (blue points in Figure 24), we compute the fraction of its area that is incorrectly classified as permanently shadowed. This "false positive fraction"

in Figure 24 approaches zero with increasing area (i.e., the false positive rate has a smaller effect on larger PSRs). In the outermost tile, on average, ~50% of 1-pixel PSRs are not permanently shadowed and approximately 34/23/12% of each 5/10/100-pixel PSR is not permanently shadowed. In the innermost tile, on average, ~30% of 1-pixel PSRs are not permanently shadowed and approximately 19/12/5% of each 5/10/100-pixel PSR is not permanently shadowed.

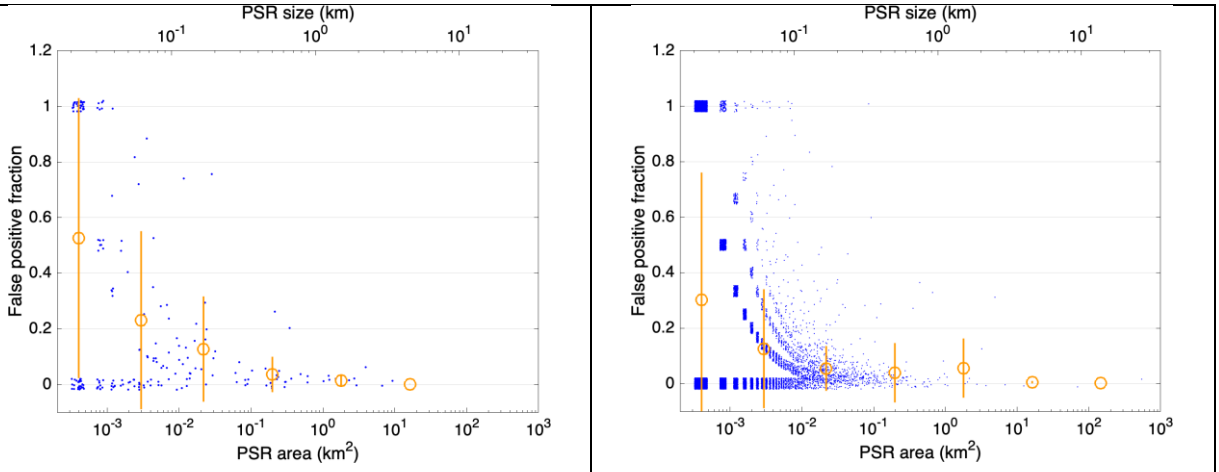

Figure 24 – Same as Figure 23, but showing the false positive rate for individual PSR pixels within PSRs of a given area. The false positive fraction is defined as the fraction of pixels within a PSR that are incorrectly classified as permanently shadowed.

6 Conclusions

Upcoming missions to the lunar south pole require detailed maps over large areas to fully characterize landing sites locally and regionally and to place their data into proper geologic context. To that end, we have produced enhanced LOLA altimetry data for the south polar region, from which we computed new maps of surface height and slope with associated uncertainties, as well as topographic roughness on horizontal baselines of 100 – 1600 m. We combined the roughness maps into a color composite image and classified every map pixel based on its roughness spectrum. These maps reveal a diversity of terrains characterized by their hectometer-scale roughness which is controlled by cratering and downslope mass transport. The south polar region is littered with linear roughness features of order ~1 – 10 km wide and ~10s – 100s of km long hypothesized to be secondary impacts within extended ejecta rays. Some of these features may pass nearby or through candidate Artemis III regions and other candidate landing sites. Non-uniformities in swath width and roughness could reflect variations in secondary impactor properties and/or target terrain properties, notably slope leading to downslope transport and surface modification. This highlights the role that impacts have had on shaping the south polar terrain even from outside the region. Therefore, future south polar missions would benefit from the systematic large-scale mapping of such extended ejecta distributions, which should also be considered when interpreting sample provenance and other in-situ/orbital data. The distribution of ejecta from these impacts can be mapped, in part, by LOLA topographic roughness.

Using the improved LOLA south polar altimetry, we also computed new 20 m/pix maps of PSRs covering 80° – 90° S. The PSR CSFD shows an approximately power-law behavior with a mean exponent of -0.77 ± 0.07 whose spread largely represents real spatial variation. Poleward of 80° S, the total PSR area is ~21,000 km^2, in good agreement with previous work. PSRs with areas < 1 km^2 contain 15% ± 5% of the total PSR area. We studied how accurately we can measure the large-scale relative frequencies of PSRs of different sizes, and for any particular PSR, the likelihood that there actually is a PSR there, and the accuracy of its area. The measured PSR CSFD is generally lower than the true one at small PSR sizes. All else being equal, the completeness rate decreases as PSR size decreases because smaller PSRs are more likely to lie in gaps between LOLA spots. Since the LOLA spot density decreases (effective resolution worsens) with distance from the pole, the PSR CSFD completeness rate also decreases farther from the pole. Incompleteness has a relatively small effect on the CAFD since smaller PSRs contribute progressively less to that distribution. Most measured PSR areas tend to be underestimates of the true areas likely due to the incomplete sampling of the surface inherent in the LOLA spot distribution. The magnitude of the underestimate is relatively insensitive to effective resolution. Finally, the fraction of pixels within a PSR that are incorrectly classified as permanently shadowed decreases with PSR size and increases as effective resolution worsens. At the lowest LOLA spot

densities averaged over scales of ~80 km in the PSR map near 80° S, the false positive fraction and fractional area error can rise to ~50% for the smallest (1 pixel) PSRs.

The new maps presented here have many applications in the scientific study and exploration of the lunar south polar region. They can aid in the geologic mapping of the region (e.g., Bernhardt et al. 2020; Krasilnikov et al. 2023) which informs landing site characterization, sample provenance, and the interpretation of other in-situ and remote sensing data. They will aid in planning traverses for which it is important to know the topography and slopes (Basilevsky et al. 2019; Mazarico et al. 2023) as well as the locations of PSRs to avoid or target for science measurements. They will also be useful for many upcoming missions besides Artemis III, such as VIPER (Volatiles Investigating Polar Exploration Rover; Colaprete et al. 2022) and KPLO (Korea Pathfinder Lunar Orbiter) with ShadowCam (Robinson et al. 2018), for the mapping and modeling of PSRs, cold traps, and polar volatiles.

Appendix

The height difference between any two closely-spaced laser spots can be approximated as being due to their physical separation, geolocation errors, and range error. We take a Monte Carlo approach and compute the height of each random spot as,

$$z = \mathcal{U}(0,1)\tan\theta + \mathcal{N}(\sigma_v^2) + \mathcal{N}(\sigma_h^2)\tan\theta + \mathcal{N}(\sigma_r^2)$$

where $\mathcal{U}(0,1)$ is a uniformly-distributed random deviate on the interval [0, 1 m], $\mathcal{N}(\sigma^2)$ is a zero-mean normally-distributed random deviate with variance σ^2, and θ is the local topographic slope. In this model, the along- and cross-track geolocation errors are assumed equal. Thus, the RMS vertical and single-axis horizontal geolocation errors are σ_v and σ_h, respectively. The RMS range error, σ_r, is proportional to the RMS return pulse width, σ_{pw}, for which Gardner (1992) developed a model that increases with topographic slope according to

$$\sigma_{pw}^2 = \sigma_t^2 + \sigma_f^2 + \sigma_s^2$$

$$\sigma_{pw}^2 = \sigma_t^2 + \sigma_f^2 + \sigma_m^2 + \frac{4R^2}{c^2}[\tan^2\phi\ \tan^2\theta]$$

where σ_t is the RMS transmit pulse width (σ_t = FWHM / 2.35), σ_f is the RMS receiver impulse response, σ_s is the surface response due to footprint-scale slope and sub-footprint RMS roughness (σ_m), R is the range, c is the speed of light, and ϕ is the RMS laser beam divergence angle (half-angle at e^{-2} intensity). Neumann et al. (2003) applied the Gardner (1992) model to Mars Orbiter Laser Altimeter data to map sub-footprint roughness on Mars. Here, we neglect sub-footprint roughness and adopt LOLA-specific representative values of the other parameters: σ_t = 2 ns, σ_f = 2 ns, R = 50 km, and ϕ = 50 μrad (Smith et al. 2010; Calibration Document for the Lunar Orbiter Laser Altimeter Instrument; http://imbrium.mit.edu/CALIB/CALIBRPT.PDF). Finally, we write the RMS range error as

$$\sigma_r = \sigma_{r0}\sqrt{\left(1 + \frac{\frac{4R^2}{c^2}[\tan^2\phi\ \tan^2\theta]}{\sigma_t^2 + \sigma_f^2}\right)}$$

where the nominal LOLA range error over flat slopes σ_{r0} = 0.1 m (Smith et al. 2010). We generate ~100,000 spot pairs with separations < 1 m and compute the median and interquartile range of their absolute z differences.

622

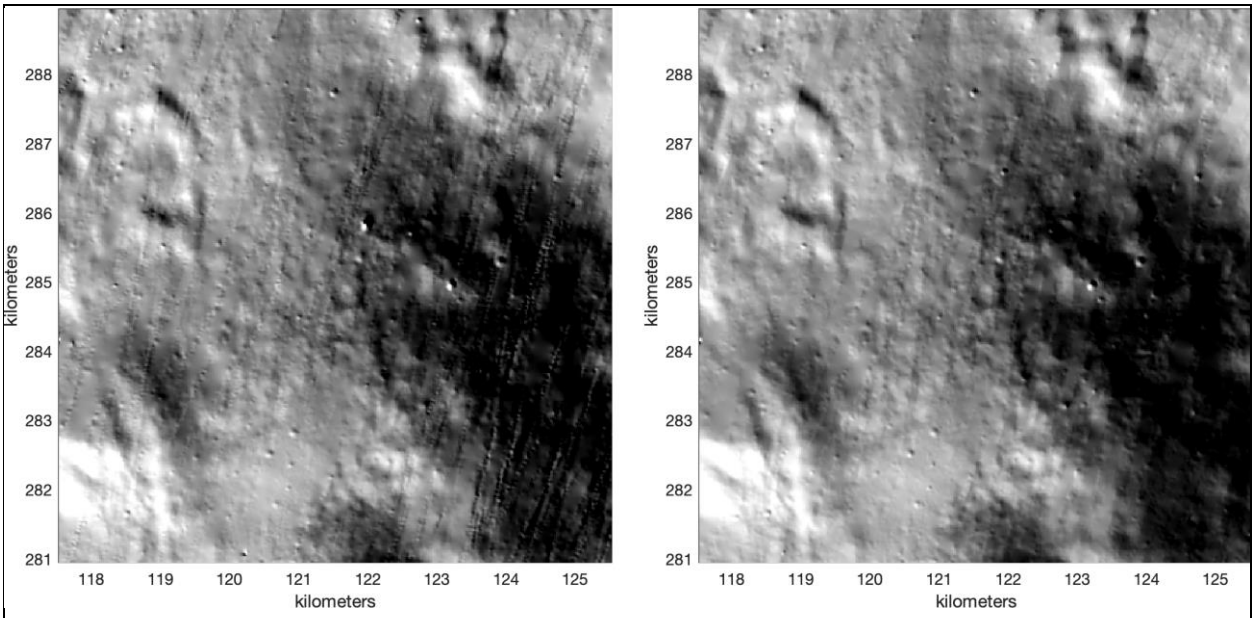

Figure A1 – Hillshade of old (left) and new (right) 20 m/pix LDEM.

623

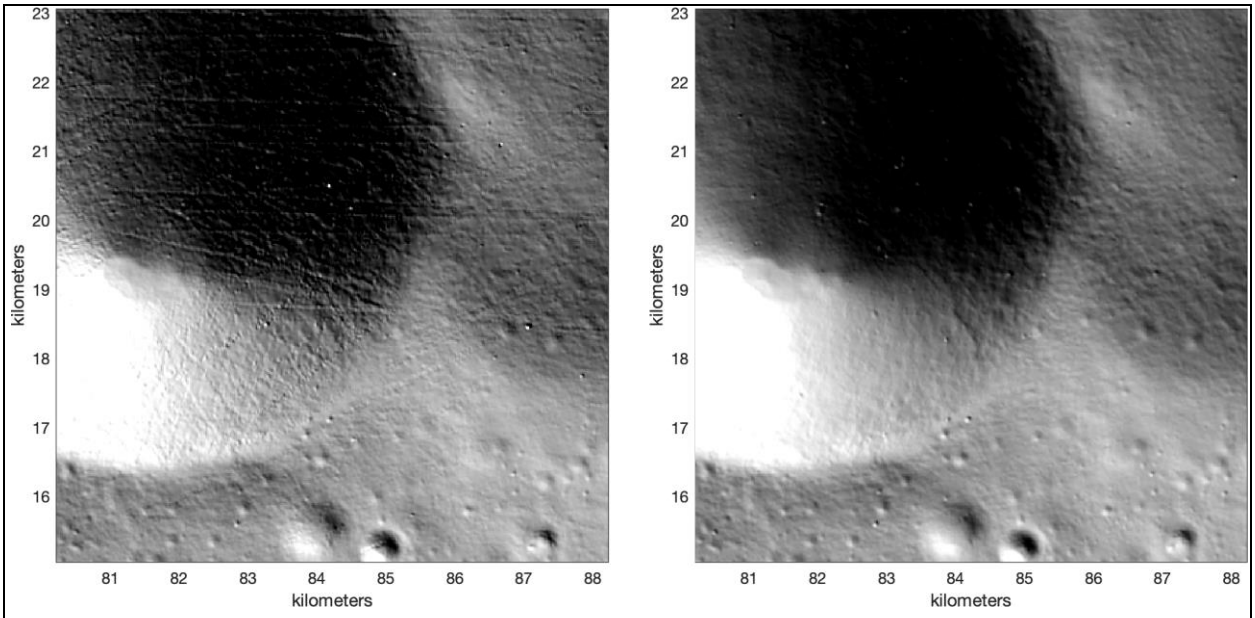

Figure A2 – Hillshade of old (left) and new (right) 20 m/pix LDEM.

624
625

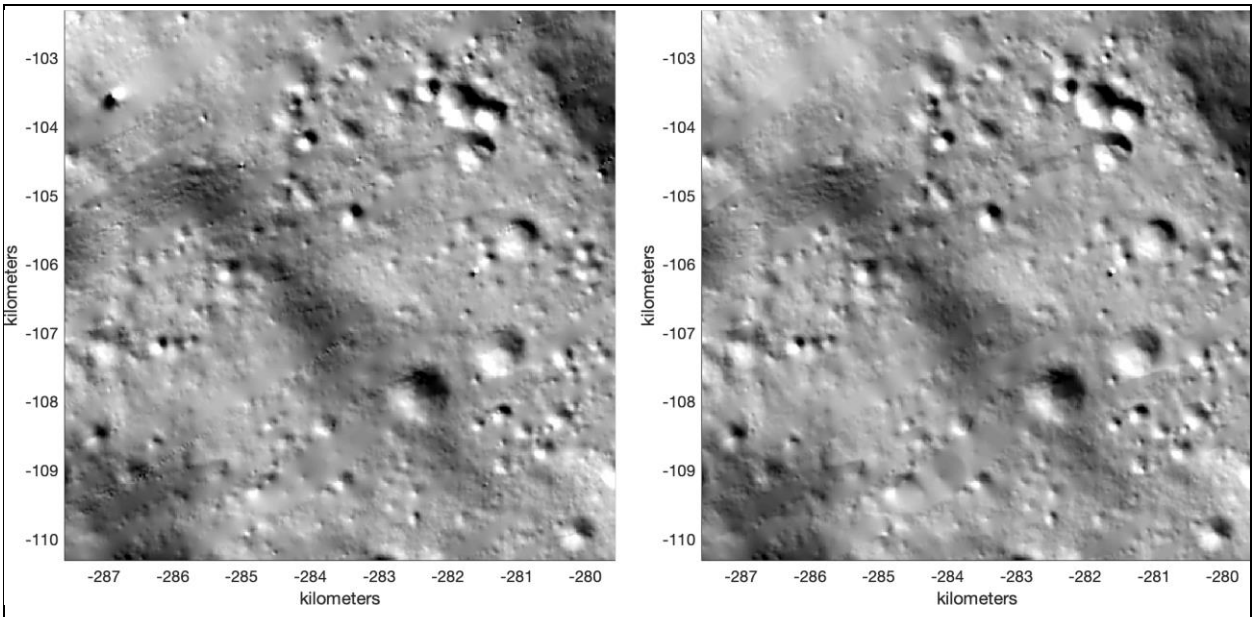

Figure A3 – Hillshade of old (left) and new (right) 20 m/pix LDEM.

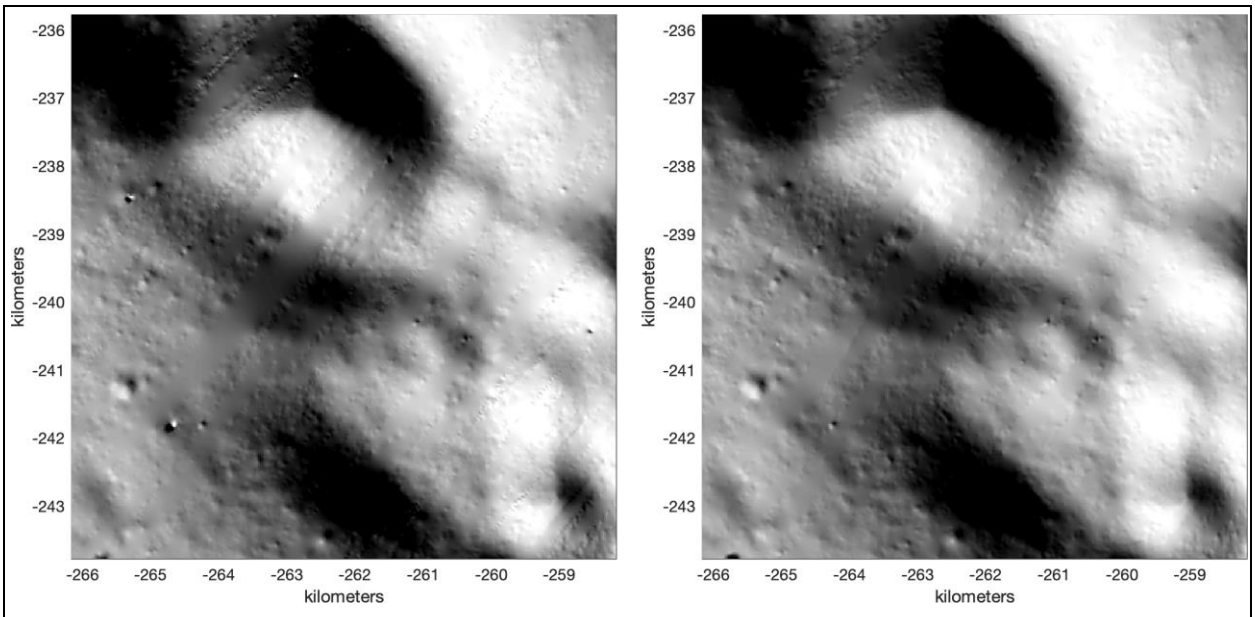

Figure A4 – Hillshade of old (left) and new (right) 20 m/pix LDEM.

631
632

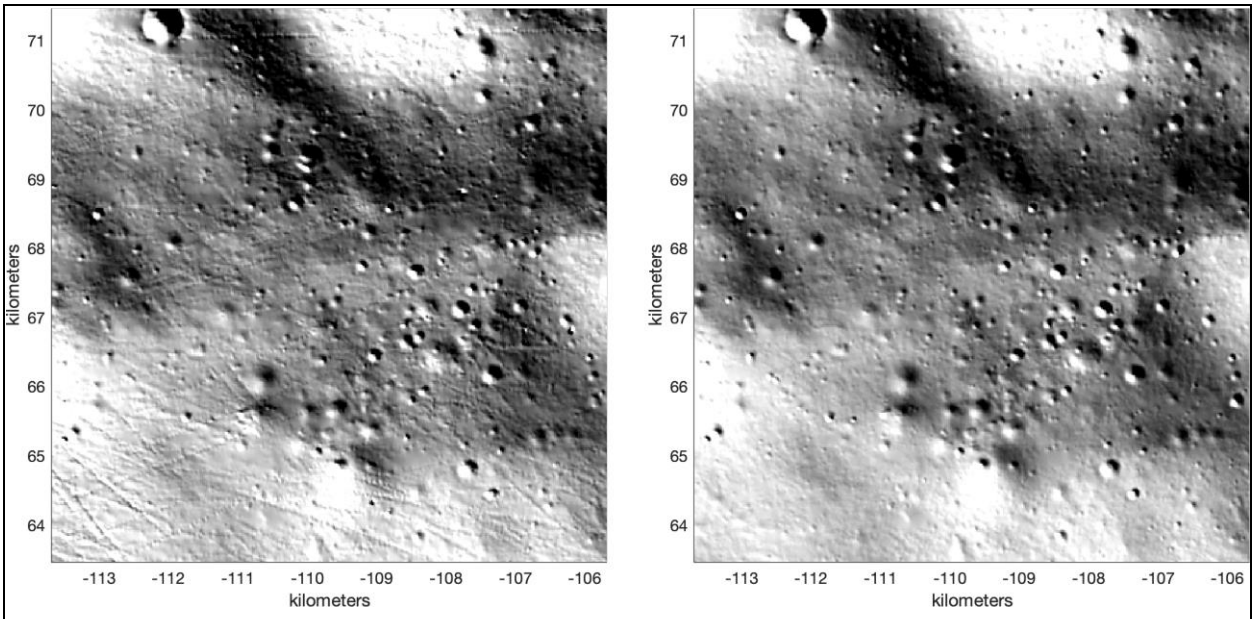

Figure A5 – Hillshade of old (left) and new (right) 20 m/pix LDEM.

633

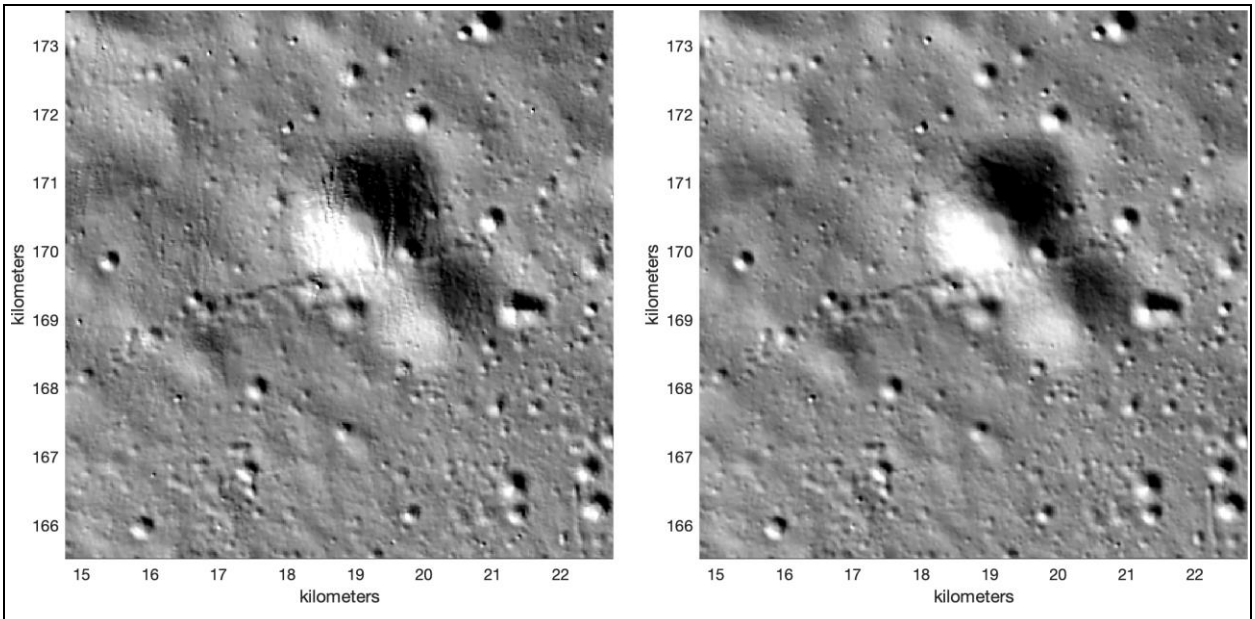

Figure A6 – Hillshade of old (left) and new (right) 20 m/pix LDEM.

634
635

636
637

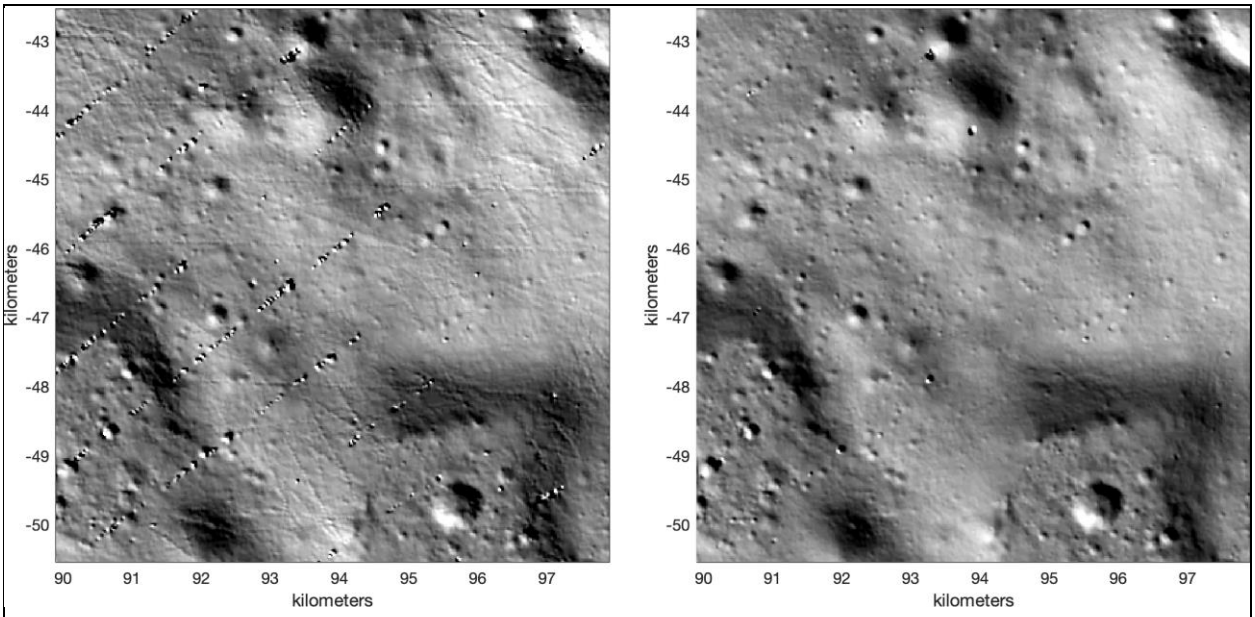

Figure A7 – Hillshade of old (left) and new (right) 20 m/pix LDEM.

638

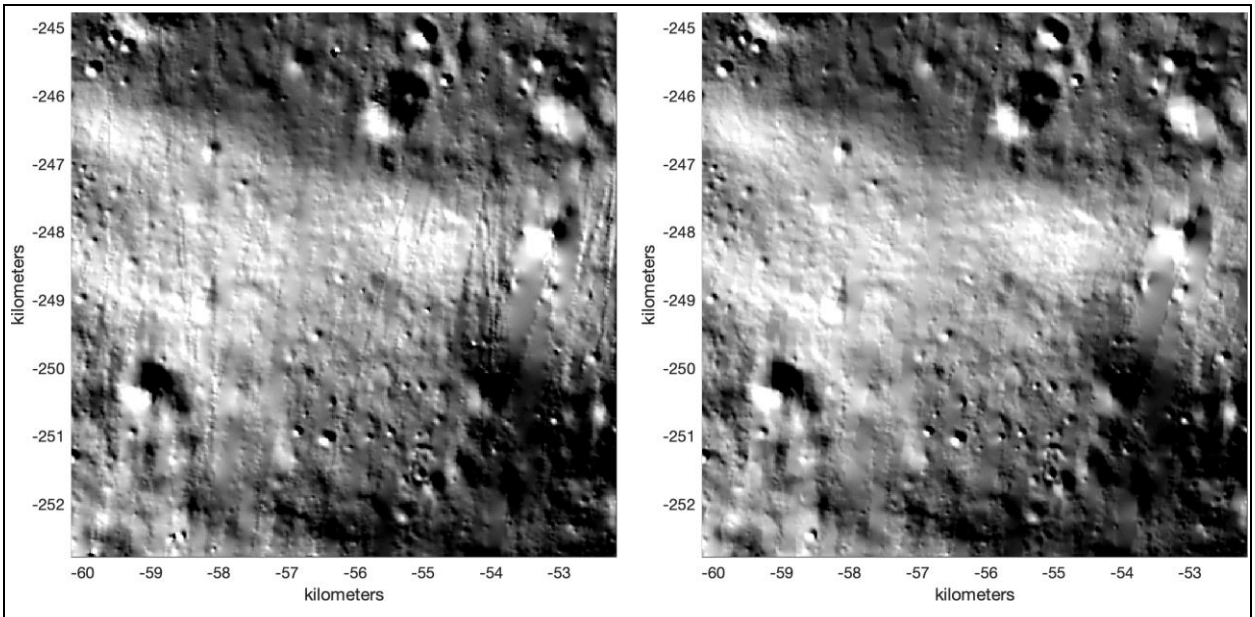

Figure A8 – Hillshade of old (left) and new (right) 20 m/pix LDEM.

639
640

641
642

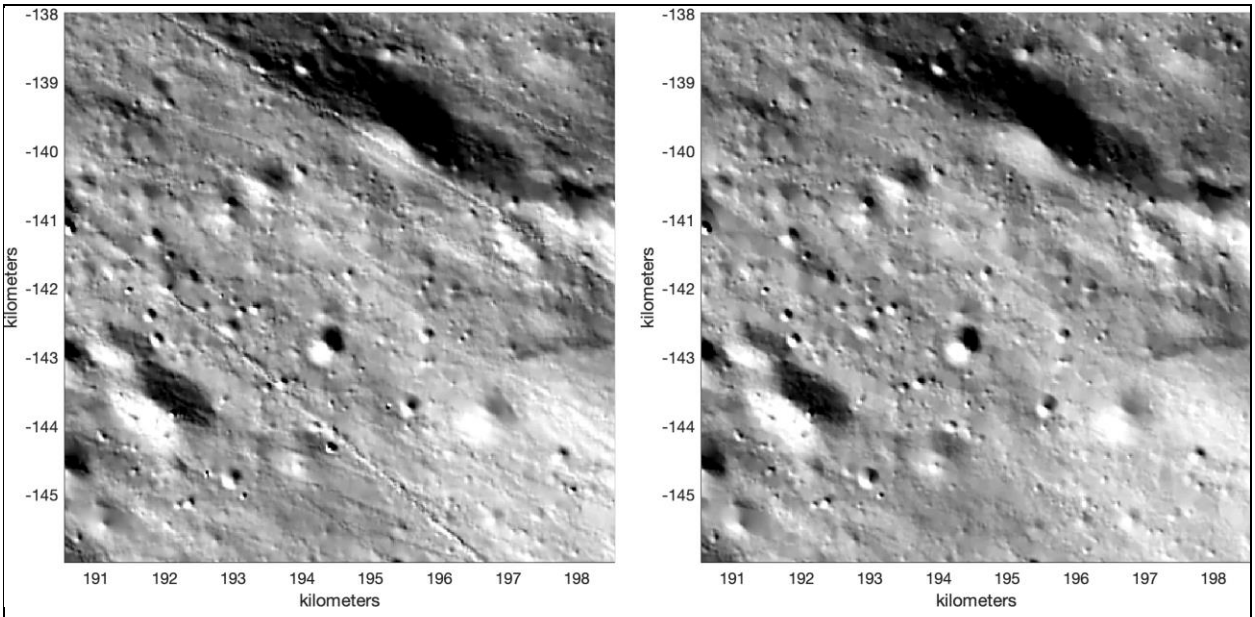

Figure A9 – Hillshade of old (left) and new (right) 20 m/pix LDEM.

643

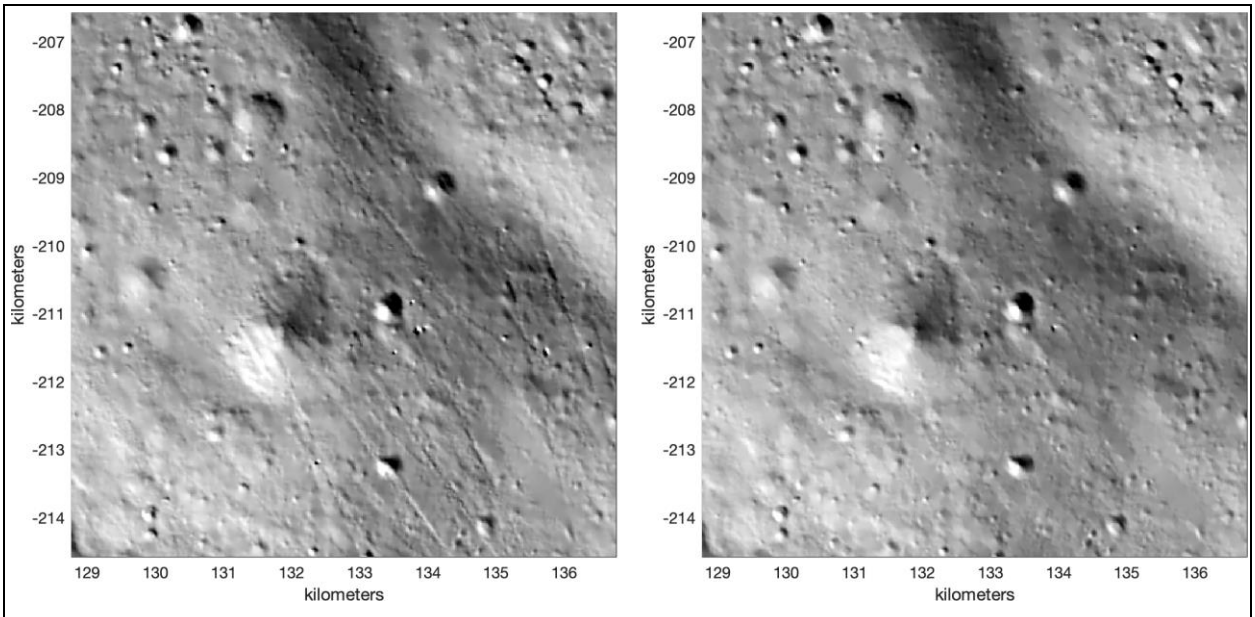

Figure A10 – Hillshade of old (left) and new (right) 20 m/pix LDEM.

644
645

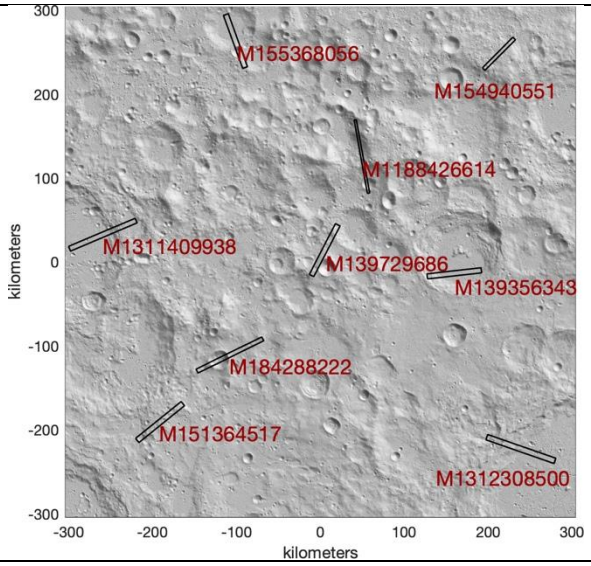

Figure A11 – Hillshade of LDEM showing the locations of NAC images in Figures 3 – 4 and A12 – A18.

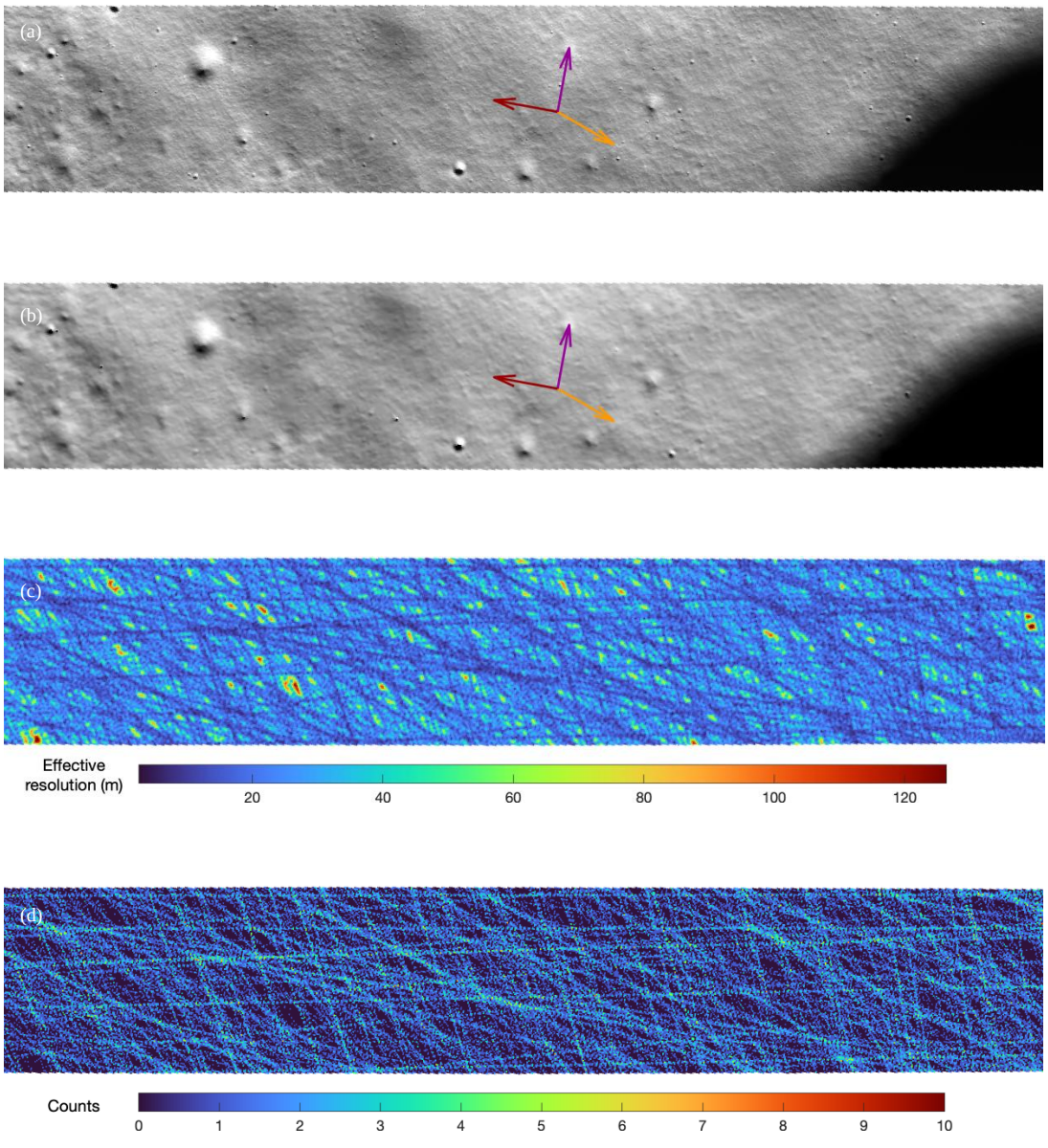

Figure A12 – (a) Sub-region of a 20 m/pix map-projected NAC image M1188426614, (b) 20 m/pix rendered LDEM, (c) LDEM effective resolution in meters, (d) LDEM counts/pix. The **1 km**-long arrows indicate the direction to the south pole (orange) and stereographic +X/+Y (purple/brown).

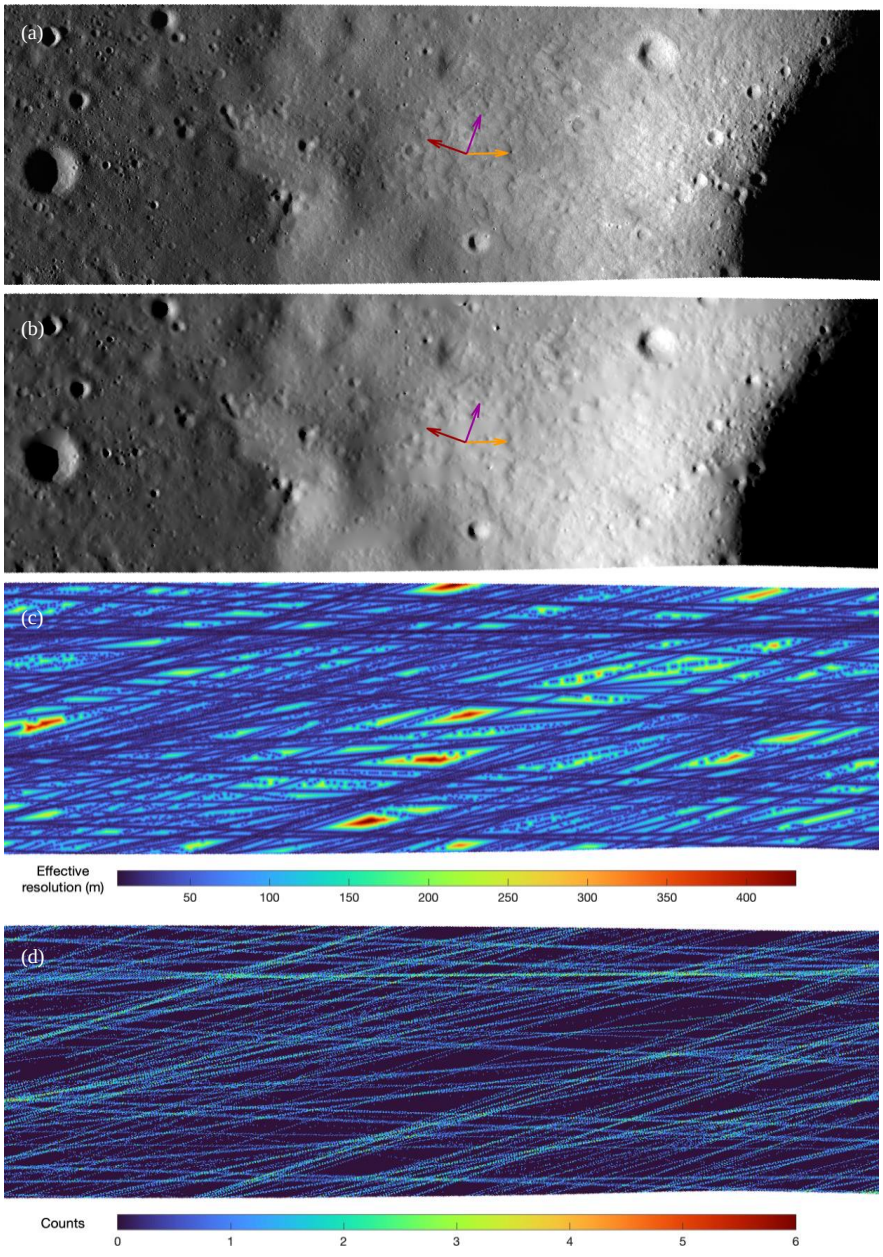

Figure A13 – Same as Figure A12, but for NAC image M155368056.

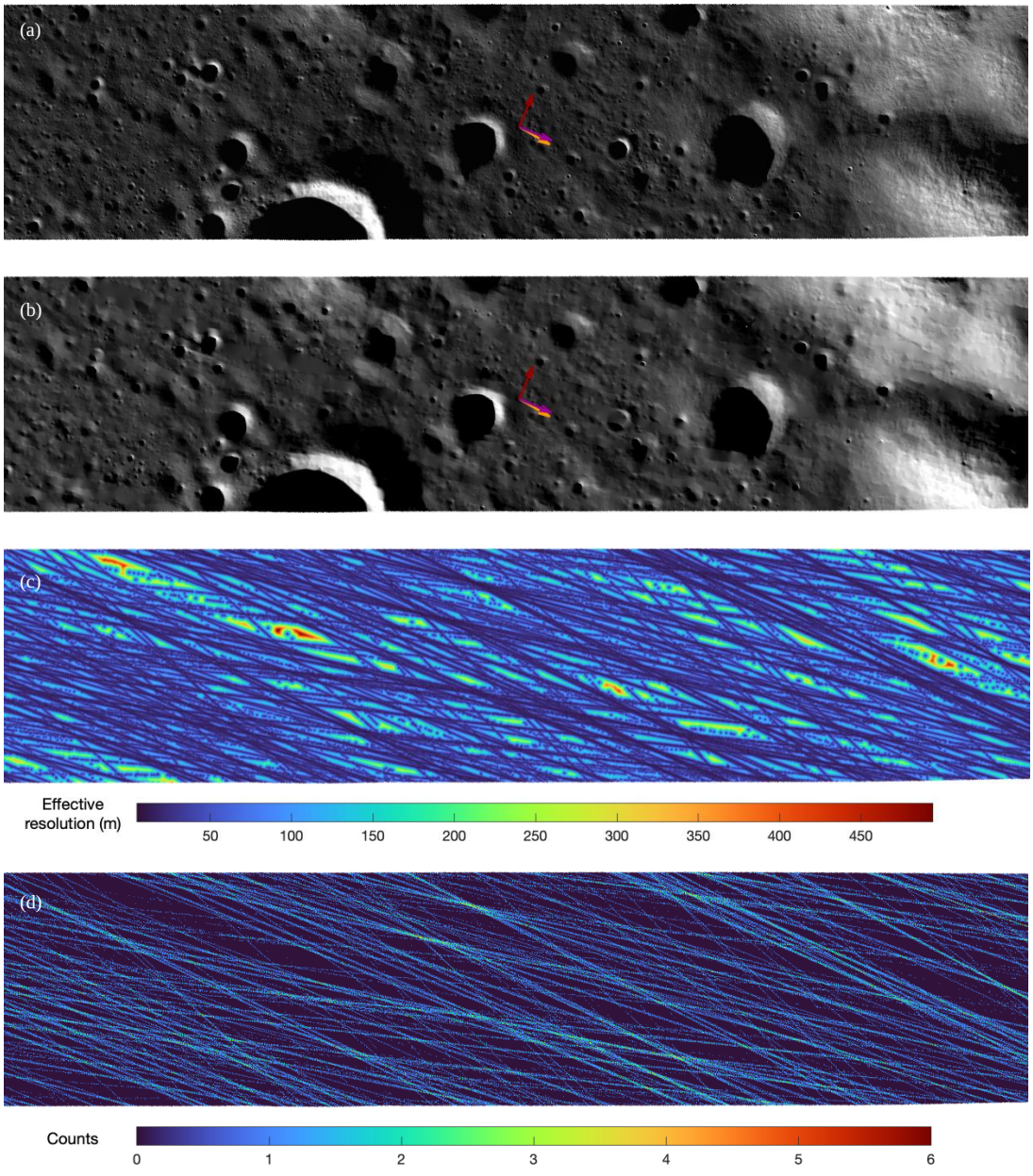

Figure A14 – Same as Figure A12, but for NAC image M1311409938.

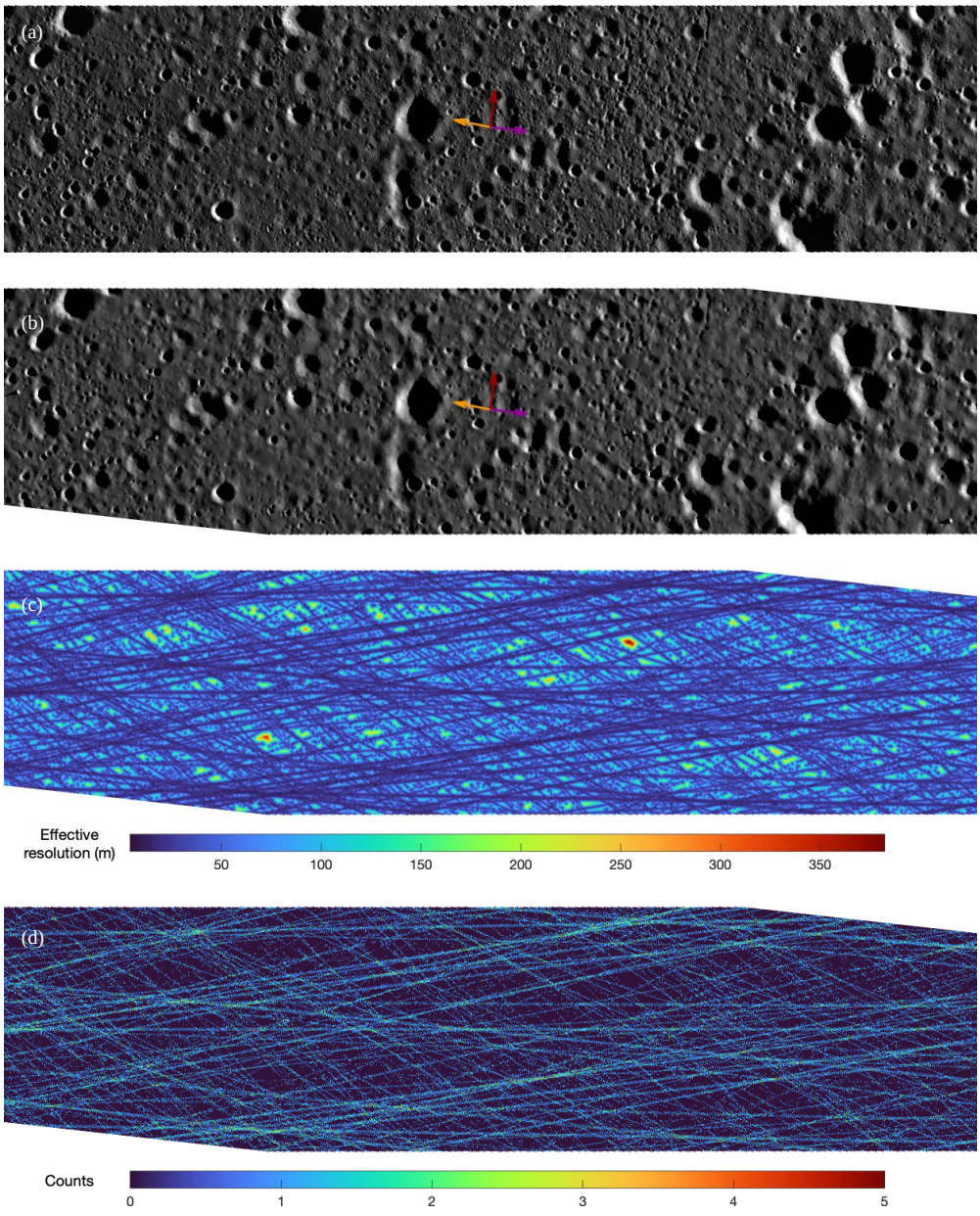

Figure A15 – Same as Figure A12, but for NAC image M139356343.

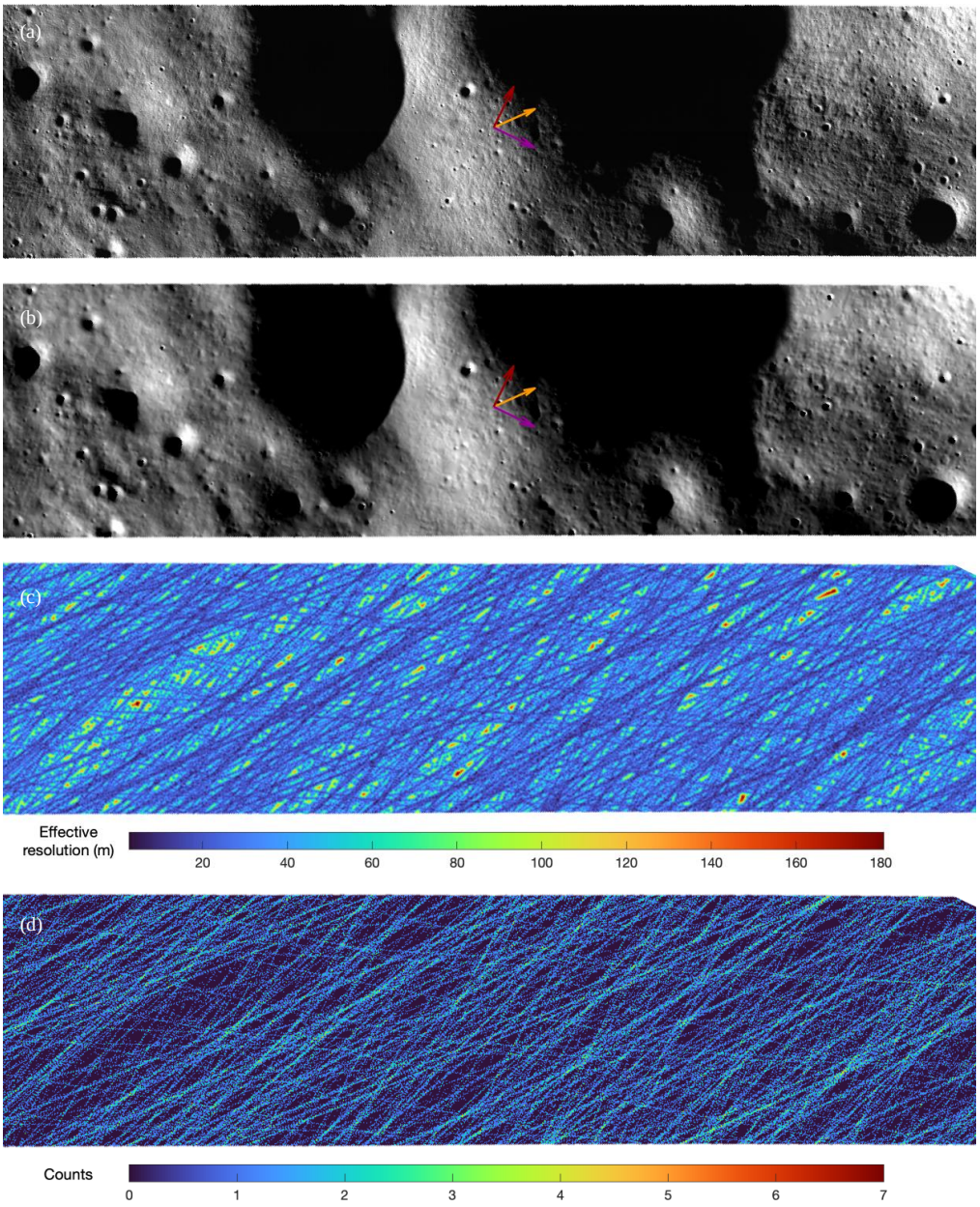

Figure A16 – Same as Figure A12, but for NAC image M184288222.

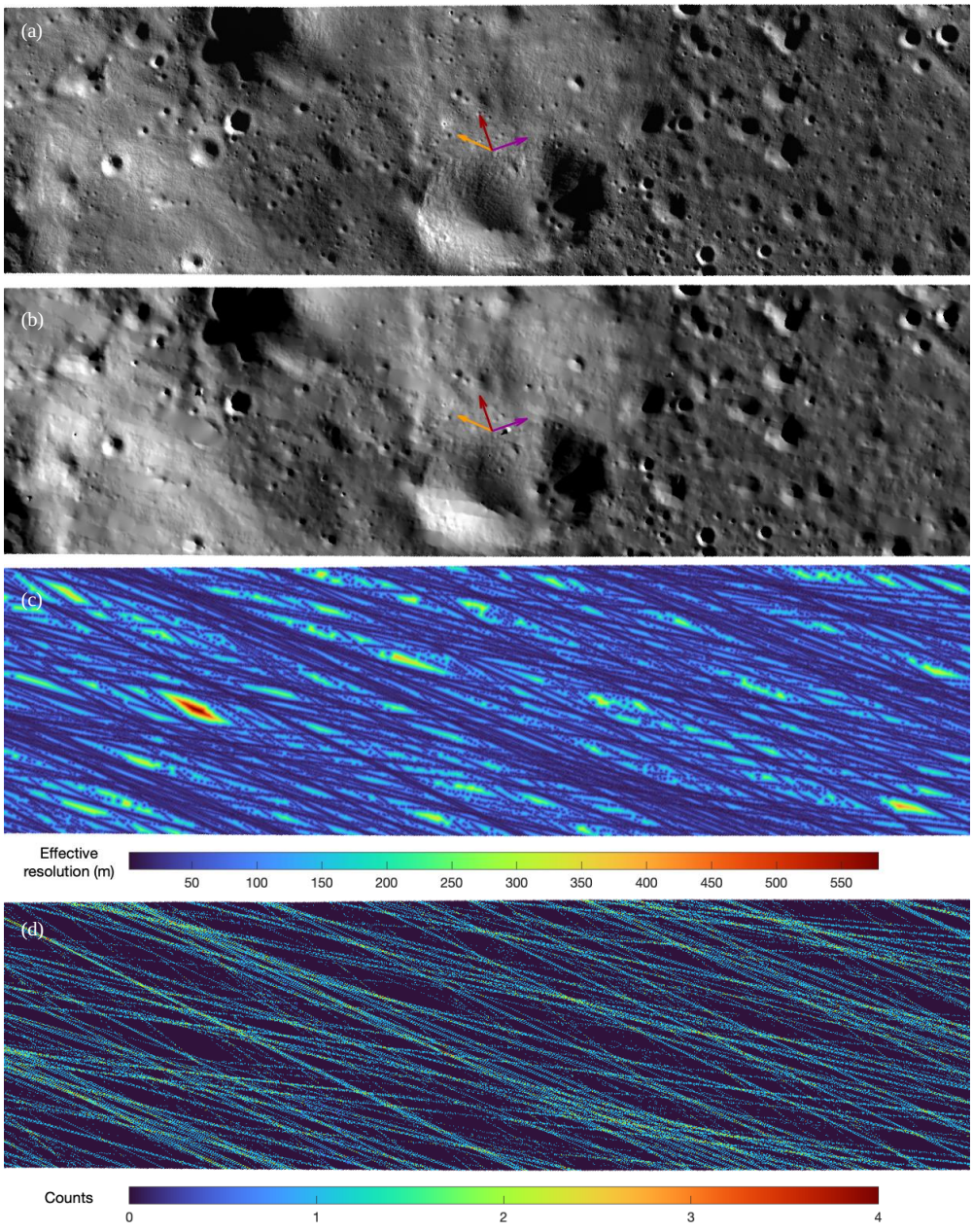

Figure A17 – Same as Figure A12, but for NAC image M1312308500.

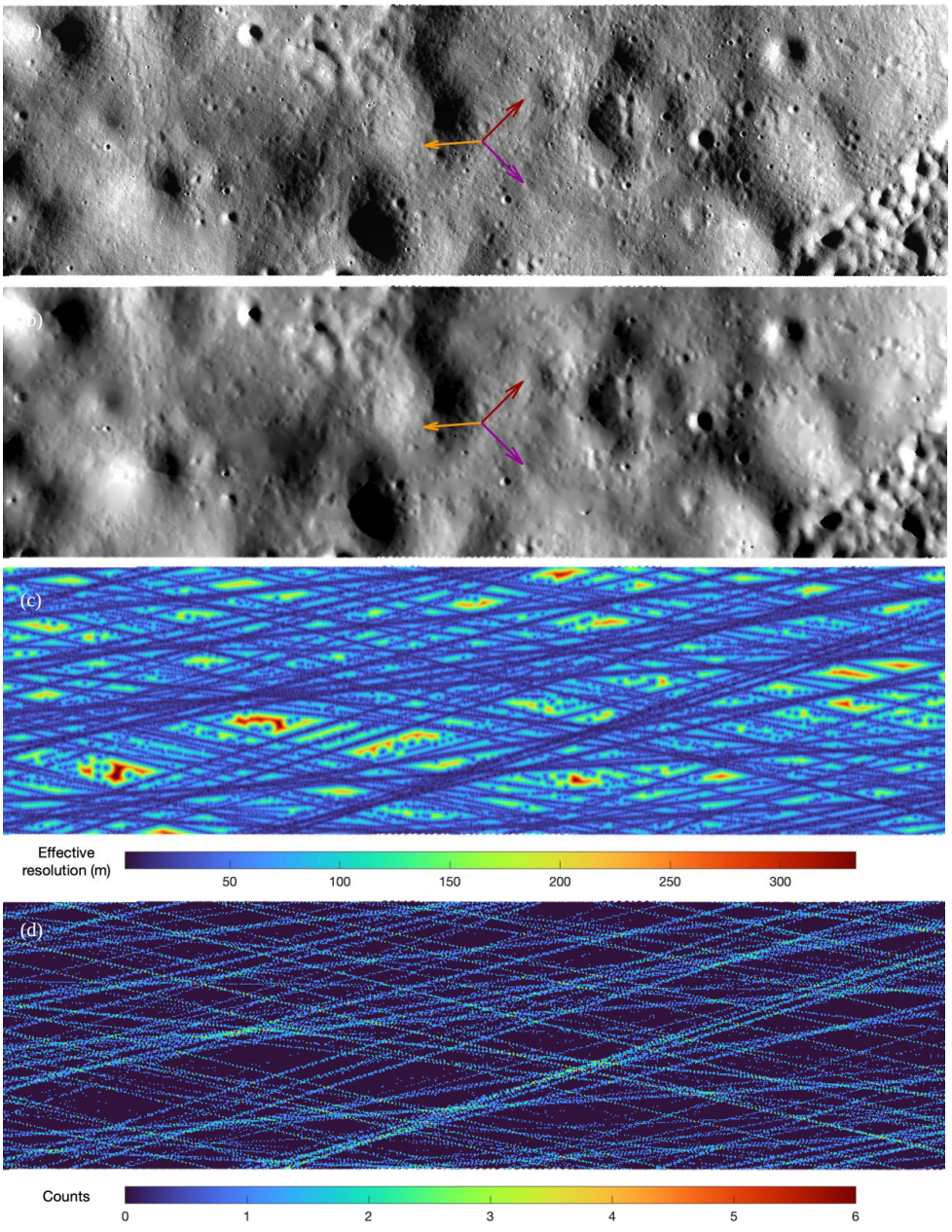

Figure A18 – Same as Figure A12, but for NAC image M154940551.

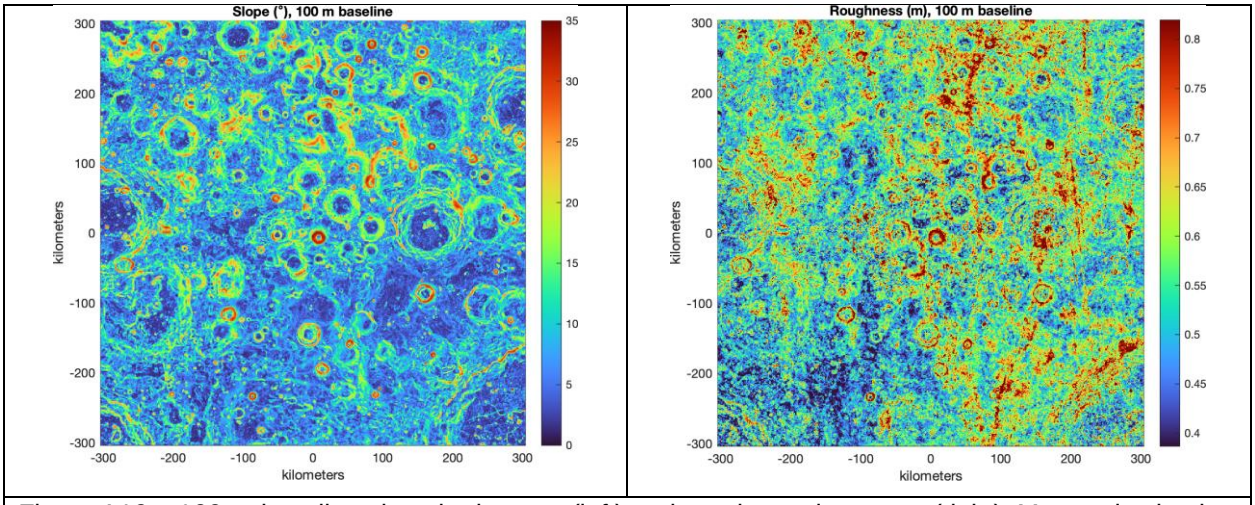

Figure A19 – 100 m-baseline slope in degrees (left) and roughness in meters (right). Map projection is stereographic centered at the pole. The roughness color scale ranges from the 2nd to the 98th percentile.

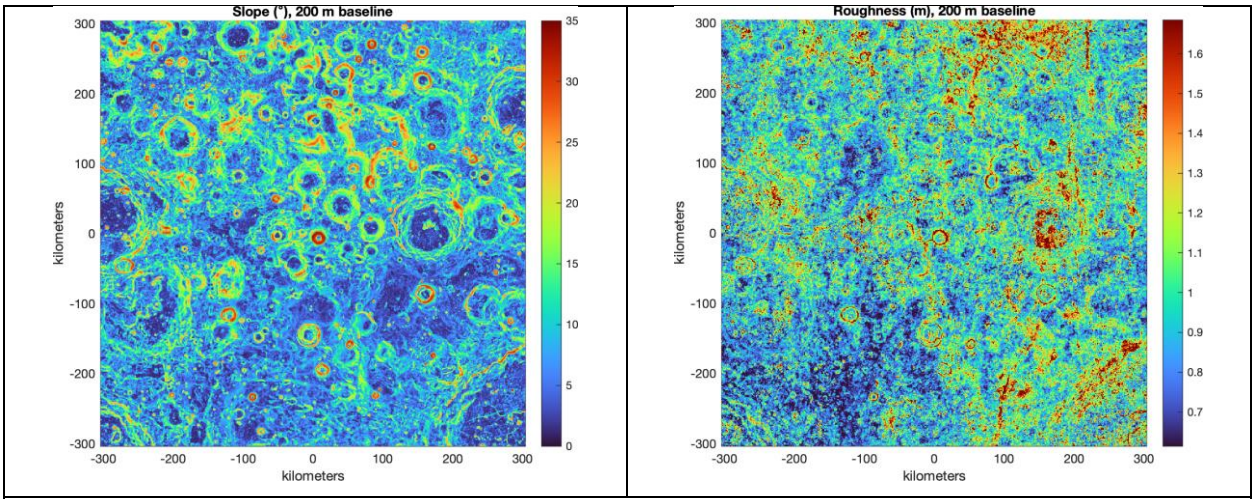

Figure A20 – Same as Figure A19, but for a 200 m baseline.

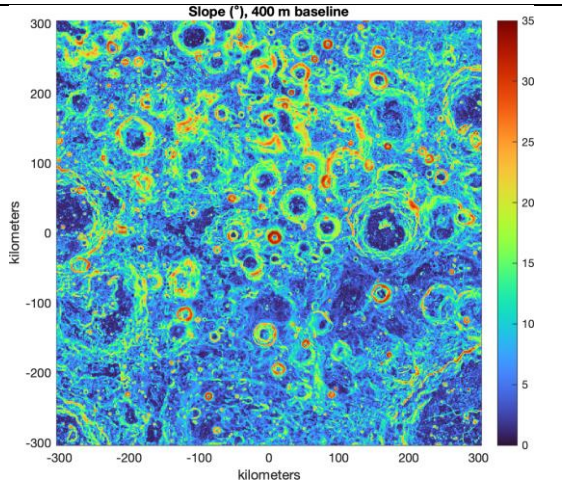

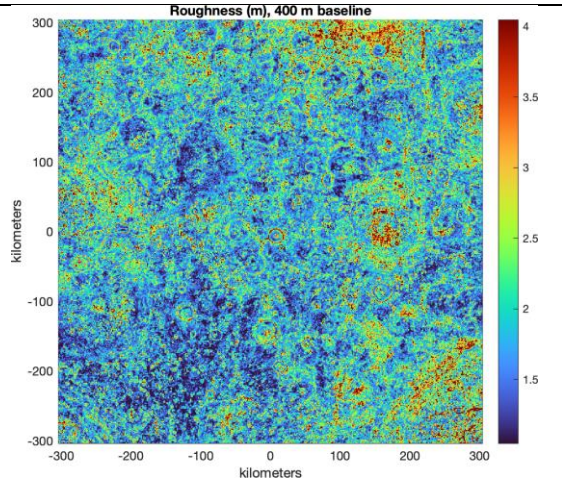

Figure A21 – Same as Figure A19, but for a 400 m baseline.

681

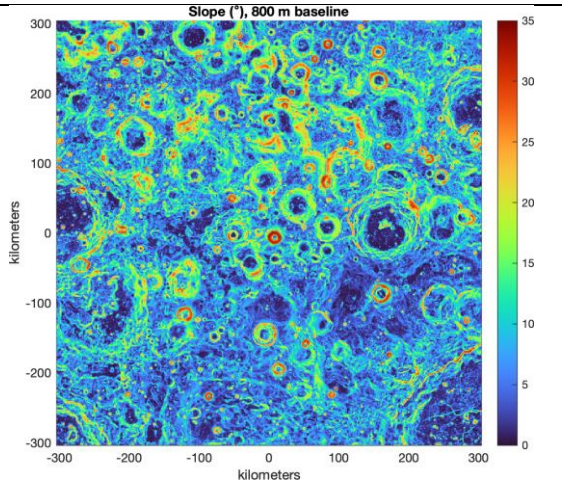

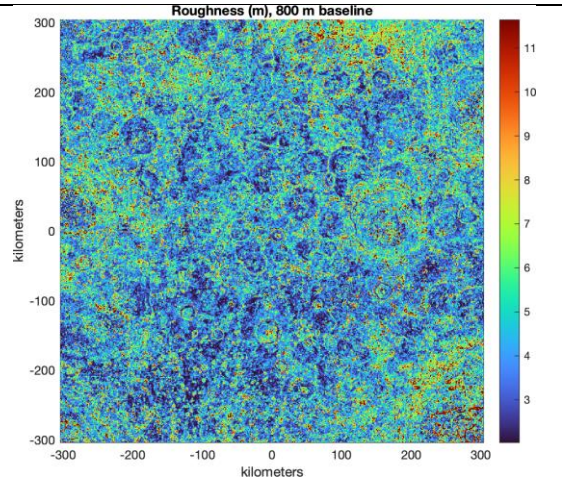

Figure A22 – Same as Figure A19, but for a 800 m baseline.

682

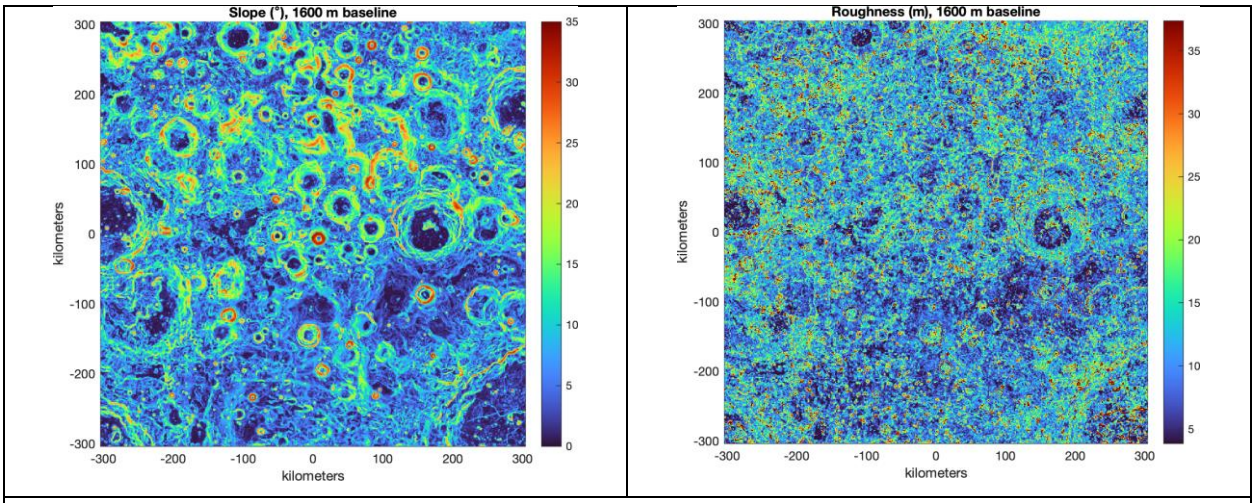

Figure A23 – Same as Figure A19, but for a 1600 m baseline.

683

684

685

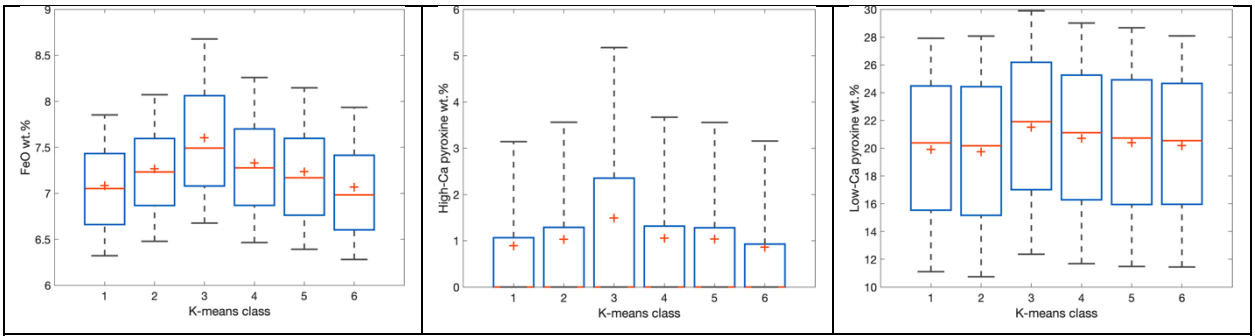

Figure A24 – Box plots of FeO (left), high-Ca pyroxene (middle), and low-Ca pyroxene (right) for the k-means classes. Each box shows the median (horizontal line), mean (plus symbol), interquartile range (box edges), and 9th/91st percentiles (whiskers).

686

687

688

689

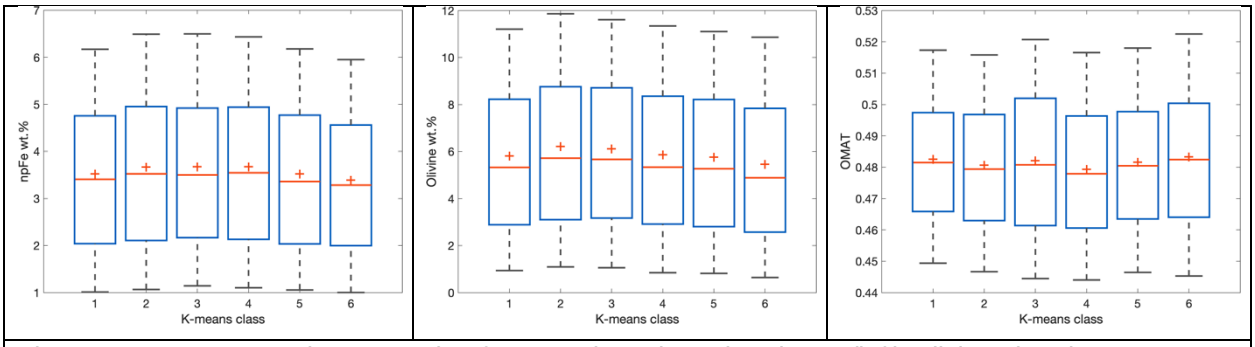

Figure A25 – Same as Figure A24, but for nanophase iron abundance (left), olivine abundance (middle), and optical maturity (OMAT; right).

690

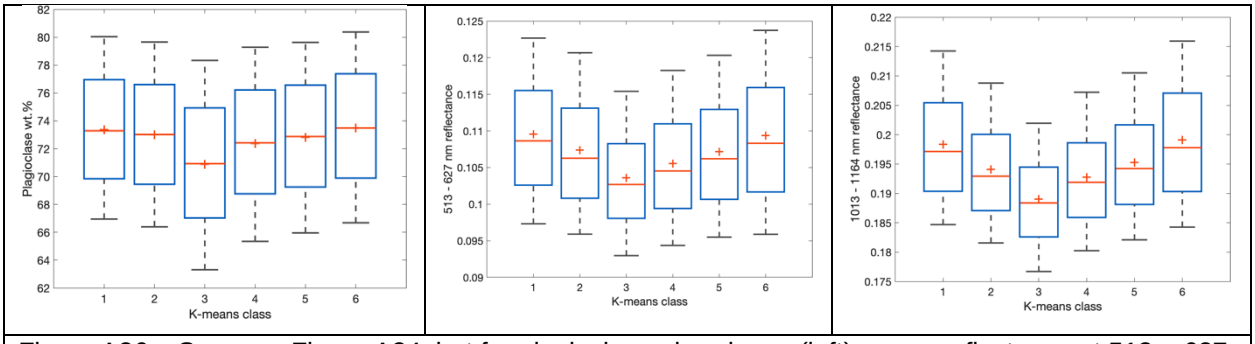

Figure A26 – Same as Figure A24, but for plagioclase abundance (left), mean reflectance at 513 – 627 nm (middle), and mean reflectance at 1013 – 1164 nm (right).

691

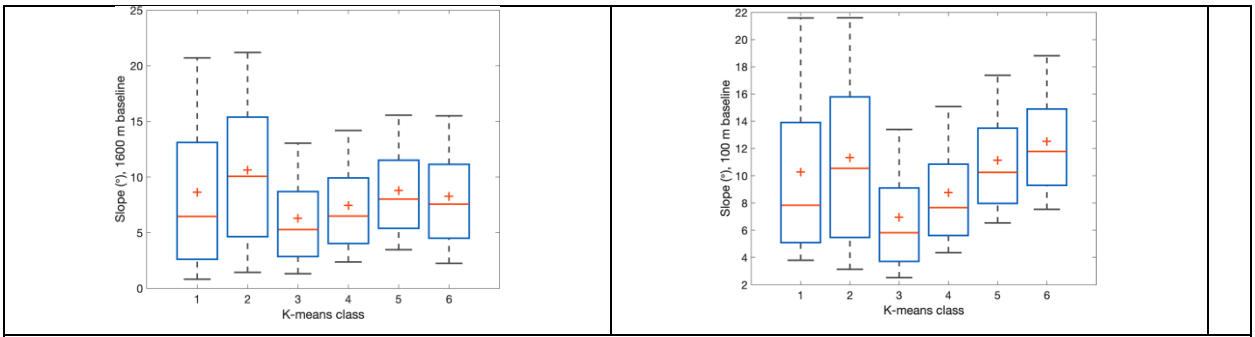

Figure A27 – Same as Figure A24, but for 1600 m-baseline slope (left) and 100 m-baseline slope (right).

692

693

694

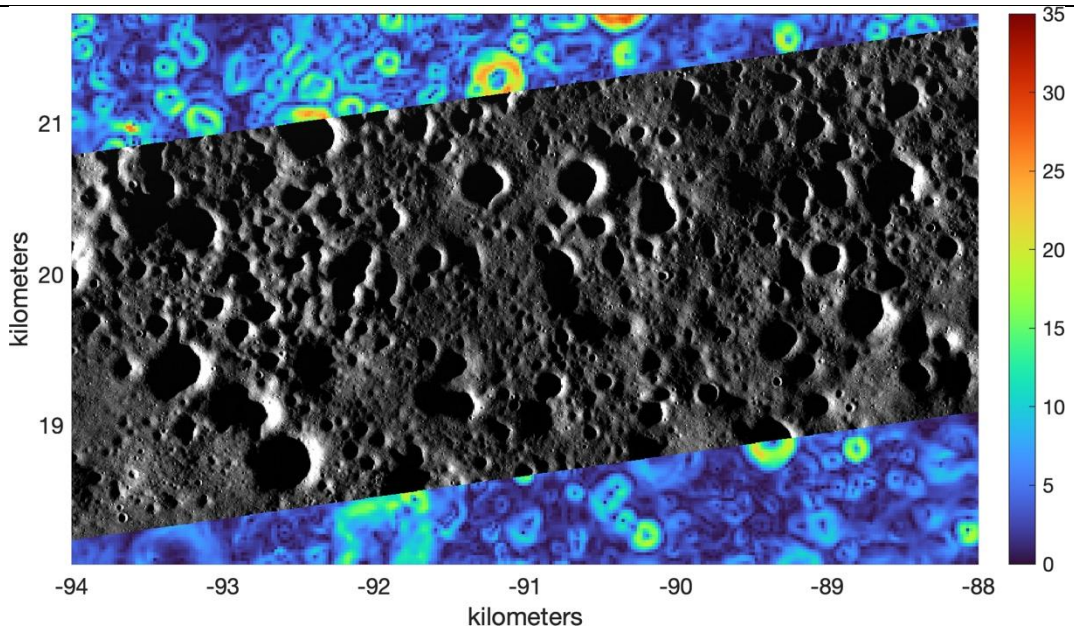

Figure A28 – LROC NAC image M140550700L showing an example of low-topographic-slope class 1 terrain. The background image is 20 m/pix topographic slope.

695
696

697

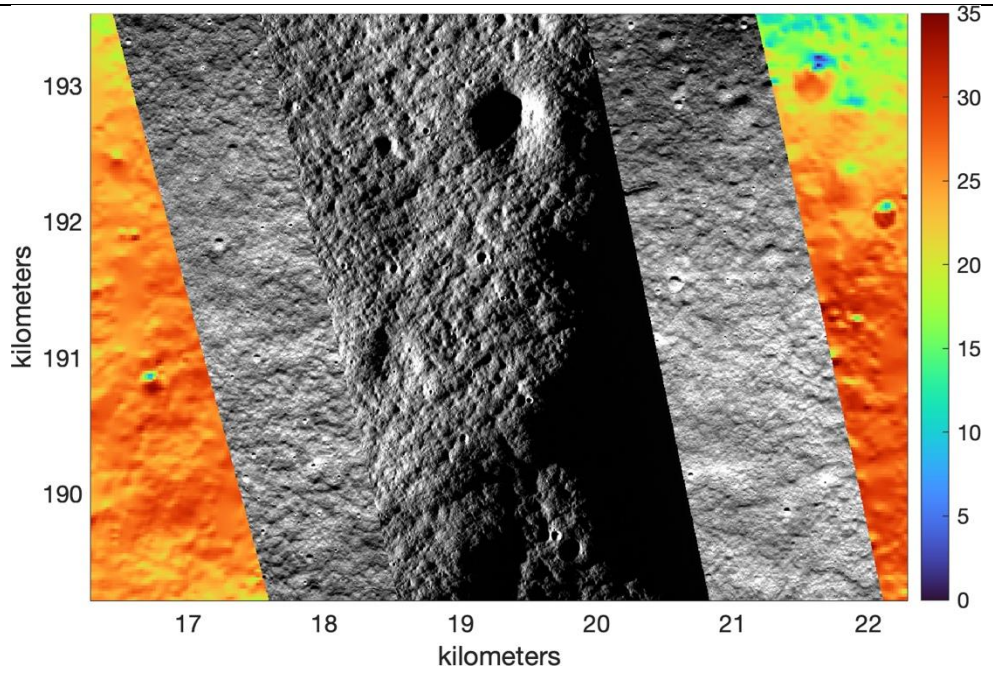

Figure A29 – LROC NAC image M1157836519R overlaid on image pair M1164904395L/R showing an example of high-topographic-slope class 1 terrain on a north-facing slope near longitude 0°. M1157836519R has a subsolar longitude ~270° (to approximate the illumination in Figure A28) and M1164904395L/R has a subsolar longitude ~0°. High-topographic-slope class 1, as in this figure, tends to be significantly less cratered than low-topographic-slope class 1 (Figure A28) while exhibiting elephant-hide texture. The background image is 20 m/pix topographic slope.

698

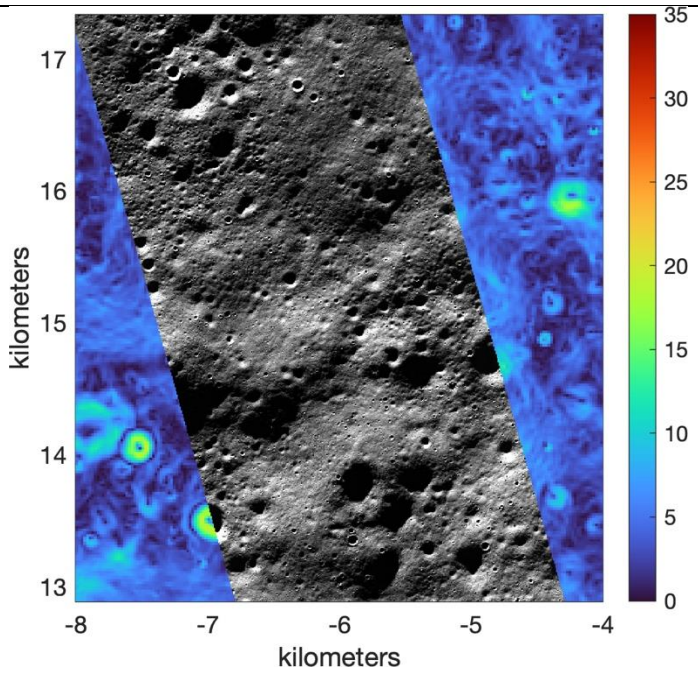

Figure A30 – LROC NAC image M140007876R showing an example of low-topographic slope class 3 terrain. The background image is 20 m/pix topographic slope.

699

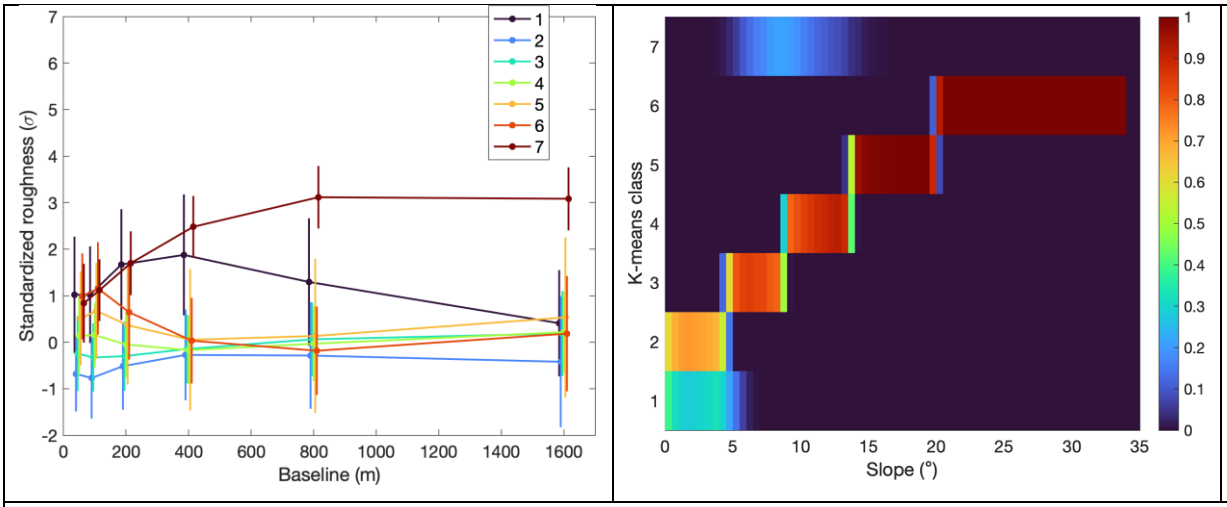

Figure A31 – Results of alternative k-means classification scheme using 1600-m baseline slope in addition to the multi-baseline roughness. Left: Roughness spectra of alternative k-means classes. Right: Resulting distribution of alternative k-means classes as a function of 1600-m baseline slope. See Figures A28, A29, and A30 for examples of alternative k-means class 1, 6, and 2, respectively.

700

Acknowledgments

Support for this research was provided by NASA's Planetary Science Division Research Program, through ISFM work package Planetary Geodesy at Goddard Space Flight Center, and by NASA's Space Technology Mission Directorate Game Changing Development Program through the Lunar DEM, Mapping, Modeling, and Validation (LuNaMaps) project. Resources supporting this work were provided by the NASA High-End Computing (HEC) Program through the NASA Center for Climate Simulation (NCCS) at Goddard Space Flight Center. We acknowledge the use of LROC imagery from Lunar QuickMap (https://quickmap.lroc.asu.edu), a collaboration between NASA, Arizona State University & Applied Coherent Technology Corporation.

Data Availability

The LOLA data used here will be publicly available at the Goddard Space Flight Center Planetary Geodynamics Data Archive (https://pgda.gsfc.nasa.gov/) and the LOLA PDS node (https://imbrium.mit.edu/). LROC data are available at the LROC PDS archive (http://lroc.sese.asu.edu/).

References

Abramov, O. & McEwen, A. 2004, International Journal of Remote Sensing, 25, 669, https://doi.org/10.1080/01431160310001599006.

Acton, C. H. 1996, Planetary and Space Science, 44, 65. https://doi.org/10.1016/0032-0633(95)00107-7.

Acton, C. H., Bachman, N., Semenov, B., Wright, E. 2017, Planetary and Space Science, 150, 9. https://doi.org/10.1016/j.pss.2017.02.013.

Barker, M. K., Mazarico, E., Neumann, G. A., et al. 2021, Planetary and Space Science, 203, 105119. https://doi.org/10.1016/j.pss.2020.105119.

Basilevsky, A. T., Krasilnikov, S. S., Ivanov, M. A., et al. 2019. Solar System Research, 53, 383. https://doi.org/10.1134/S0038094619050022.

Bater, C. W. & Coops, N. C. 2009, Computer & Geosciences , 35, 289. https://doi.org/10.1016/j.cageo.2008.09.001.

Bernhardt, H., Robinson, M. S. & Boyd, A. K. 2022, Icarus, 379, 114963. https://doi.org/10.1016/j.icarus.2022.114963.

Beyer, R. A., Alexandrov, O. & McMichael, S. 2018, Earth and Space Science, 5, 9, 537.

https://doi.org/10.1029/2018EA000409.

Cai, Y. & Fa, W. 2020, JGRE, 125, 8. https://doi.org/10.1029/2020JE006429.

Colaprete, A., Elphic, R. C., Shirley, M., et al. 2022, 53rd Lunar and Planetary Science Conference, 2678, 2675.

Denevi, B. W. & Robinson, M. S. 2020, LSSW, 2241, 5122.

Deutsch, A. N., Head, J. W., Neumann, G. A., et al. 2020, GRL, 47, 15, e87782. https://doi.org/10.1029/2020GL087782.

Deutsch, A. N., Heldmann, J. L., Colaprete, A., et al. 2021, PSJ, 2, 213. https ://doi.org/10.3847/PSJ/ac24ff.

Folkner, W. M., Williams, J. G. & Boggs, D. H. 2009, Interplanetary Network Prog. Rep., 42, 1.

Gardner, C. S., IEEE Transactions on Geoscience and Remote Sensing, 30, 1061. https://doi.org/10.1109/36.175341.

Gläser, P., Oberst, J., Neumann, G. A., et al. 2018, Planetary & Space Science, 162, 170, https://doi.org/10.1016/j.pss.2017.07.006.

Hayne, P. O., Aharonson, O. & Schörghofer, N. 2021, Nature Astronomy, 5, 169. https://doi.org/10.1038/s41550-020-1198-9.

Heldmann, J. L., Colaprete, A., Elphic, R. C., et al. 2016, Acta Astronautica, 127, 308. https://doi.org/10.1016/j.actaastro.2016.06.014.

Huber, P. J., Robust Statistics, 1981, John Wiley, New York.

James, P. B., Smith, D. E., Byrne, P. K., et al. 2019, GRL, 46, 10, 5100. https://doi.org/10.1029/2019GL082252.

Kramer, G. Y., Kring, D. A., Nahm, A. L. et al. 2013, Icarus, 223, 131. https://doi.org/10.1016/j.icarus.2012.11.008.

Krasilnikov, S. S., Ivanov, M. A., Head, J. W., et al. 2023, Icarus, 394, 115422. https://doi.org/10.1016/j.icarus.2022.115422.

Kreslavsky, M. A., Head, J. W., Neumann, G. A., et al. 2013, Icarus, 226, 52. https://doi.org/10.1016/j.icarus.2013.04.027.

Kreslavsky, M. A., Bondarenko, N. V. & Head, J. W. 2021, 52nd Lunar and Planetary Science Conference, 2548, 1826.

Lawrence, D. J., Feldman, W. C., Elphic, R. C., et al. 2002, JGRE, 107, E12, https://doi.org/10.1029/2001JE001530.

764 Lemelin, M., Lucey, P. G., & Camon, A. 2022, PSJ, 3, 63. https://doi.org/10.3847/PSJ/ac532c.

765 Lemelin, M., Daly, M. G. & Deliège, A. 2020, JGRE, 125, 1. https://doi.org/
766 10.1029/2019JE006105.

767 Lemelin, M., Lucey, P. G., Neumann, G. A., et al. 2016a, Icarus, 273, 315.
768 https://doi.org/10.1016/j.icarus.2016.02.006.
769 Lemelin, M., Lucey, P. G., Trang, D., et al. 2016b, American Geophysical Union, Fall General
770 Assembly 2016, P52B-04.
771 Lemoine, F. G., Goossens, S., Sabaka, T. J., et al. 2014, GRL, 41, 3382.
772 https://doi.org/10.1002/2014GL060027.
773 Leys, C., Ley, C., Klein, O., et al. 2013, J. Exp. Soc. Psychol., 49, 764,
774 https://doi.org/10.1016/j.jesp.2013.03.013.

775 Lloyd, S. P. 1982, IEEE Transactions on Information Theory, 28, 129.
776 https://doi.org/10.1109/TIT.1982.1056489.
777 Mazarico, E., Neumann, G. A., Smith, D. E., et al. 2011, Icarus, 211, 2, 1066.
778 https://doi.org/10.1016/j.icarus.2010.10.030.
779 Mazarico, E., Neumann, G. A., Barker, M. K., et al. 2018, Planetary and Space Science, 162, 2.
780 https://doi.org/10.1016/j.pss.2017.10.004.

781 Mazarico, E., Barker, M. K., Jagge, A. M., et al. 2023, Acta Astronautica, 204, 49.
782 https://doi.org/10.1016/j.actaastro.2022.12.023.

783 Moon, S., Paige, D. A., Siegler, M. A. & Russell, P. S. 2021, GRL, 48, e90780.
784 https ://doi.org/10.1029/2020GL090780.

785 National Academies Of Science, Engineering, and Medicine, 2022, Washington, DC: The
786 National Academies Press. https://doi.org/10.17226/26522.

787 Neumann, G. A., Abshire, J. B., Aharonson, O., et al. 2003, GRL, 30.
788 https://doi.org/10.1029/2003GL017048.

789 Neumann, G. A., Gläser, P. A., Hiesinger, H., et al. 2015, 46th Lunar and Planetary Science
790 Conference, 1832, 2218.

791 Pavlis, D. E. & Nicholas, J. B. 2017, GEODYN II system description (Vols. 1–5), contractor report
792 SGT Inc; Greenbelt, MD.

793 Robinson, M. S. & ShadowCam Team 2018, Lunar Polar Volatiles, 2087, 5028.

Rosenburg, M. A., Aharonson, O., Head, J. W., et al. 2011, JGR, 116, E2. https://doi.org/10.1029/2010JE003716.

Rubanenko, L., Venkatraman, J. & Paige, D. A. 2019, NatGe., 12, 597. https://doi.org/10.1038/s41561-019-0405-8.

Sibson, R. 1981, In Interpolating multivariate data, New York: John Wiley & Sons, pp. 21-36.

Smith, D. E., Zuber, M. T., Jackson, G. B., et al. 2010, Space Science Reviews, 150, 209. https://doi.org/10.1007/s11214-009-9512-y.

Smith, D. E., Zuber, M. T., Neumann, G. A., et al. 2017, Icarus, 283, 70. https://doi.org/10.1016/j.icarus.2016.06.006.

Tye, A. R., Fassett, C. I., Head, J. W., et al. 2015. Icarus, 255, 70. https://doi.org/10.1016/j.icarus.2015.03.016.

Wang, J., Kreslavsky, M. A., Liu, J., et al. 2020, JGRE, 125, 10, e06091. https://doi.org/10.1029/2019JE006091.

Wells, K. S., Campbell, D. B., Campbell, B. A., et al. 2010, JGR, 115, E6, https://doi.org/10.1029/2009JE003491.

Wessel, P., Smith, W. H. F., Scharroo, R., et al. 2013, EOS Trans. AGU, 94, 45, 409. https://doi.org/10.1002/2013EO450001.

Williams, J. G., Boggs, D. H. & Folkner, W. F. 2008, DE421 Lunar Orbit, Physical Librations, and Surface Coordinates, IOM 335-JW,DB,WF-20080314-001.

Wilson, L. & Head, J. W., 2018, Icarus, 305, 105. https://doi.org/10.1016/j.icarus.2017.12.030.

Xiao, Z., Zeng, Z., Ding, N., et al. 2013, Earth and Planetary Science Letters, 376, 1. https://doi.org/10.1016/j.epsl.2013.06.015.

Yokota, Y., Gwinner, K., Oberst, J., et al. 2014, GRL, 41, 5, 1444. https://doi.org/10.1002/2013GL059091.

Zharkova, A. Y., Kreslavsky, M. A., Head, J. W., et al. 2020, Icarus, 351, 113945. https://doi.org/10.1016/j.icarus.2020.113945.

Zuber, M. T., Head, J. W., Smith, D. E., et al. 2012, Nature, 486, 378. https://doi.org/10.1038/nature11216